

Normal fault evolution and coupled landscape response: examples from the Southern Apennines, Italy

Duna C. Roda-Boluda and Alexander C. Whittaker

Department of Earth Science and Engineering, Imperial College London, London, UK

ABSTRACT

We present new data addressing the evolution, activity and geomorphic impact of three normal faults in the Southern Apennines: the Vallo di Diano, East Agri and Monti della Maddalena faults. We show that these faults have minimum total throws of *ca.* 1000–2000 m, and throw rates of *ca.* 0.7–1 mm year⁻¹ for at least the last *ca.* 18 ka. We demonstrate that for the Vallo di Diano and East Agri faults, the landscape is effectively recording tectonics, with relief, channel and catchment slopes varying along fault strike in the same manner as normal fault activity does, with little apparent influence of lithology. We therefore use these data to reconstruct the time-integrated history of fault interaction and growth. From the distribution of knickpoints on the footwall channels, we infer two episodes of base level change, which we attribute to fault interaction episodes. We reconstruct the amount of throw accumulated after each of these events, and the segments involved in each, from the fault throw profiles, and use fault interaction theory to estimate the magnitude of the perturbations and past throw rates. We estimate that fault linkage events took place 0.7 ± 0.2 Ma and 1.4 ± 0.3 Ma in the Vallo di Diano fault, and 1 ± 0.1 in the East Agri Fault, and that both faults likely started their activity between 3 and 3.5 Ma. These fault linkage scenarios are consistent with the observed knickpoint heights. This method for reconstructing fault evolution could potentially be applied for any normal faults for which there is information about throw and throw rates, and in which channels are transiently responding to tectonics.

INTRODUCTION

Study motivation

Normal faults provide excellent settings in which to study landscape response to tectonics, because slip rates can often be constrained with high temporal and spatial resolution (e.g. Roberts & Michetti, 2004; Commins *et al.*, 2005; Papanikolaou & Roberts, 2007). Moreover, we have a good knowledge of how normal fault segments grow and interact through time (e.g. Peacock & Sanderson, 1991; McLeod *et al.*, 2000; Cowie & Roberts, 2001).

Recent studies have investigated how normal fault growth and interaction controls topographic relief (e.g. Densmore *et al.*, 2004, 2007; Strak *et al.*, 2011), the evolution of drainage networks (e.g. Whittaker *et al.*, 2007; Attal *et al.*, 2011; Hopkins & Dawers, 2015) and sediment supply dynamics (e.g. Cowie *et al.*, 2006; Whittaker *et al.*, 2010). Rivers crossing normal faults are sensitive to fault activity and their long profiles can record information about the timing and magnitude of tectonic perturbations over timescales up to 10⁶ years (e.g. Commins *et al.*, 2005; Boulton & Whittaker, 2009;

Whittaker, 2012; Hopkins & Dawers, 2015). In contrast, catchment slopes are expected to grow until they reach a critical strength-limited threshold, beyond which erosion becomes landslide-dominated, and slopes become decoupled from the tectonic forcing (e.g. Montgomery & Brandon, 2002; Ouimet *et al.*, 2009; DiBiase *et al.*, 2010), limiting further relief growth (e.g. Densmore *et al.*, 2004, 2007). However, few empirical studies quantify how relief, channels and hill-slope gradients compare with the distribution of normal fault uplift before such critical threshold slopes are surpassed, and how lithology and fault interaction influences these responses (e.g. Cyr *et al.*, 2010; Whittaker, 2012).

In this article, we characterize how the geomorphology of catchments eroding the footwalls of active normal faults in the Southern Apennines, Italy, reflects their tectonic history. First, we present new data on fault total throw and throw rates for three faults (the Vallo di Diano, Monti della Maddalena and East Agri faults), based on the integration of published and new fault displacement constraints. We then use these tectonic boundary conditions to test landscape sensitivity to active tectonics across different lithologies. Finally, we combine fault interaction theory with geomorphological data to infer the evolution and linkage history of two of these faults.

Correspondence: Duna C. Roda-Boluda, Department of Earth Science and Engineering, Imperial College London, South Kensington Campus, London SW7 2AZ, UK. E-mail: d.roda-boluda12@imperial.ac.uk

Normal fault growth and linkage

To fully understand landscape response to normal faulting, it is necessary to understand how normal faults grow and link. The mechanisms of fault growth, interaction and linkage have been increasingly well-established from theoretical models and field studies (e.g. Peacock & Sanderson, 1991; Cowie & Scholz, 1992a, b; Anders & Schlische, 1994; Cartwright *et al.*, 1995; Dawers & Anders, 1995). Immediately after nucleation, faults start accumulating displacement, and when the stress concentration at their tips overcomes the yield strength, they propagate along the tip-line (Fig. 1; e.g. Peacock & Sanderson, 1991; Cowie & Scholz, 1992a, b; Gupta & Scholz, 2000). Originally, faults nucleate randomly, but their evolution is controlled by stress feedback mechanisms, so they evolve differently depending on their location with respect to the stress field (Cowie, 1998). Positive stress feedback dictates that faults located in the centre of the array and preferentially oriented along-strike will grow more rapidly and become larger, while faults located more distally in the array will decrease their activity. In individual faults, positive stress feedback also implies that the central portions of the faults will slip more readily, and therefore have greater slip rates and accumulate more displacement than the distal sectors, leading to approximately elliptical or triangular normal fault displacement profiles (Fig. 1c; Cowie, 1998; McLeod *et al.*, 2000; Cowie & Roberts, 2001). Conversely, negative stress feedback creates a “stress shadow” zone at a critical distance

across-strike from the most active faults, so across-strike faults decrease their activity and eventually die out (e.g. Cowie, 1998; Cowie & Roberts, 2001).

When the growing tips of adjacent faults, particularly those located preferentially along-strike, reach a critical distance from each other, they start to interact and may eventually link (Fig. 1f; e.g. Cartwright *et al.*, 1995; McLeod *et al.*, 2000; Gupta & Scholz, 2000; Cowie & Roberts, 2001). Faults tend to maintain their characteristic displacement/length scaling relationship (γ), so that their displacement profiles are often self-similar as they grow (Fig. 1c, f; Cowie & Scholz, 1992a, b; Anders & Schlische, 1994; Cowie & Roberts, 2001). Hence, faults growing laterally by linkage re-adjust their displacement profiles to recover the pre-linkage γ value. They do so by enhancing their slip rates to accumulate the displacement deficit: the centres of the faults experience greater slip rate changes, while the fault tips remain relatively unaffected (Fig. 1d–f; Dawers & Anders, 1995; McLeod *et al.*, 2000; Cowie & Roberts, 2001). This enhancement begins prior to segment linkage (Peacock & Sanderson, 1991; Dawers & Anders, 1995; Gupta & Scholz, 2000; Hopkins & Dawers, 2015), and continues during and after the linkage (Cartwright *et al.*, 1995; Gupta & Scholz, 2000; Commins *et al.*, 2005), so that at different stages of fault evolution the displacement profile can be transiently under- or over-displaced (Cowie & Roberts, 2001).

Based on the assumption that during linkage, fault displacement increases to recover pre-linkage γ values, and that this will be principally accommodated at the fault,

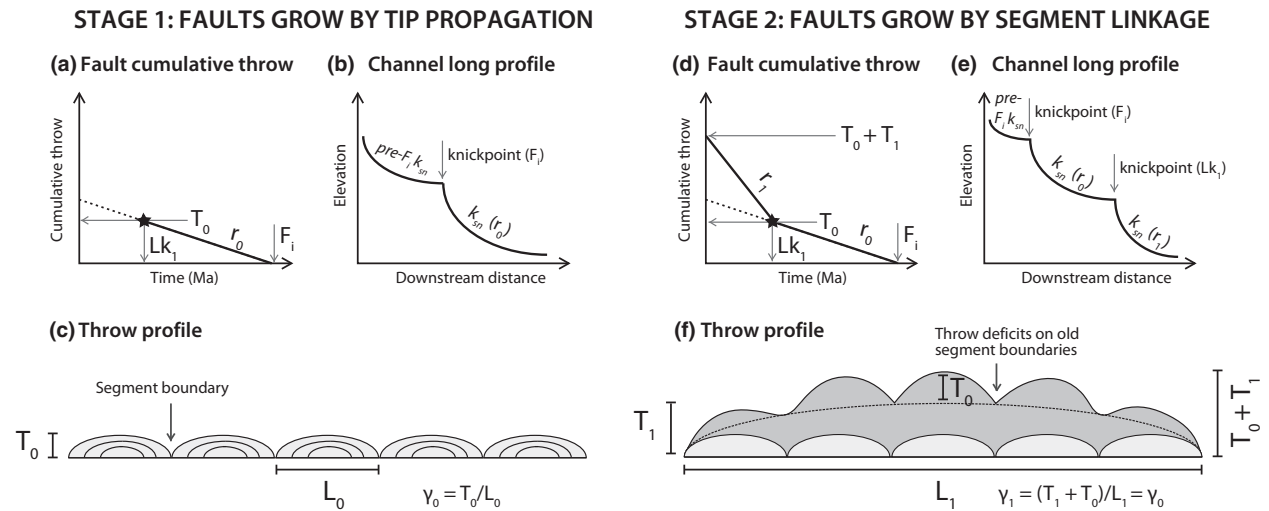


Fig. 1. Simplified growth pattern of a normal fault and normal fault array, adapted from Cowie & Roberts (2001). During the first stage (a–c), faults grow by tip propagation up to a length of L_0 , and a throw of T_0 accumulates at a rate of r_0 (a, b). Fault initiation (F_i) marks the first perturbation for channels crossing the fault and creates a knickpoint, as channels adjust their slopes from pre- $F_i k_{sn}$ to $k_{sn}(r_0)$ (b). In the following fault growth stage (d–f), the segments or faults start to link (Linkage 1, Lk_1) to create a longer structure of length L_1 , and the fault grows at a higher throw rate of r_1 (d) until it accumulates the throw necessary to achieve the same throw/length ratio (γ) as in the previous stage, T_1 . The new throw rate at the centre of the fault, r_1 is defined by $r_1 = E_1 r_0$, in which E_1 is the enhancement factor associated with Lk_1 , derived from Eqn 1 using L_0 and R_1 values (the “radius” of the new linked fault). This throw rate increase results in another knickpoint in the channel long profiles, as they incise and steepen (to a $k_{sn}(r_1)$ value) to keep pace with the new rates of base level lowering (e). After Lk_1 , the throw profile substantially changes (f), particularly in the centres of the linked fault or array, but the old segment boundaries and the throw accumulated on the previous stage, T_0 , may still be recognized.

Cowie & Roberts (2001) proposed an equation to calculate the slip rate enhancement, E , that different fault segments experience after linkage:

$$E_n = 2R_n/L_{n-1} \quad (1)$$

where L_{n-1} is the length of the n th segment before the n th linkage episode, and R_n is the distance from the centre of the n th segment to the closest linked fault tip (c.f. Cowie & Roberts, 2001; Roberts *et al.*, 2004; Fig. 1). This model makes several over-simplifications (such as assuming triangular displacement profiles, and neglecting fault overlap or interactions with across-strike or more distal faults), but it has produced valuable and plausible predictions in many cases (e.g. Cowie & Roberts, 2001; Roberts *et al.*, 2004; Boulton & Whittaker, 2009; Whittaker & Walker, 2015).

After linkage, tip propagation stops (Peacock & Sanderson, 1991; Cartwright *et al.*, 1995), so the centres of the pre-linkage segments and their segment boundaries can still be recognized, by the positions of maximum and minimum cumulative displacement zones in the footwall (Fig. 1f; Peacock & Sanderson, 1991; Dawers & Anders, 1995; Cowie & Roberts, 2001) and by depocentres and intra-basin highs in the hangingwall basin (Anders & Schlische, 1994; McLeod *et al.*, 2000). Throughout faulting history, displacement deficits at former segment tips can be sustained or obliterated depending on the 3D geometry of the segments and breached faults (Faure-Walker *et al.*, 2009).

In principle, the timing, location and magnitude of these interactions lead to temporal and spatial changes in fault slip rates, which will exert a significant control on landscape morphology, particularly with respect to channels draining between fault segment boundaries (c.f. Commins *et al.*, 2005). Hence, the process of fault growth and linkage represents an important opportunity to quantify landscape response to tectonics, because it is possible to estimate slip rate changes through time and space. However to date, relatively few studies have characterised landscape response to tectonics explicitly within the context of fault growth and interaction theory (c.f. Densmore *et al.*, 2004, 2007; Hopkins & Dawers, 2015; Whittaker & Walker, 2015).

Landscape response to normal faulting

Upland rivers are sensitive to tectonics and set the boundary conditions for hillslope steepening and relief development (Whipple & Tucker, 1999; DiBiase *et al.*, 2010; Kirby & Whipple, 2012). Their geometry is often well-described by the well-known family of stream power erosion “laws” (e.g. Whipple & Tucker, 2002; Wobus *et al.*, 2006a; Kirby & Whipple, 2012; D’Arcy & Whittaker, 2014). In these cases, channel slope, S , is related to drainage area, A , by a power law, which dictates that channels in topographic steady-state exhibit a concave up profile

that represents the erosional balance between downstream increase in discharge and decrease in gradient. For a simple stream power model, we can write:

$$S = \left(\frac{U}{K}\right)^{\frac{1}{n}} A^{\frac{m}{n}} \quad (2)$$

where U is an uplift rate, K is a coefficient that includes bedrock erodibility and other factors, and m and n are positive exponents related to the dominant erosional process and hydraulic geometry (e.g. Whipple & Tucker, 2002). The term $\left(\frac{U}{K}\right)^{\frac{1}{n}}$ can be represented by the channel steepness index, k_s , and the ratio of m/n by the channel concavity, θ . A reference value of θ is often used to estimate a normalized channel steepness index, k_{sn} , allowing comparisons between channels with different concavities (e.g. Snyder *et al.*, 2000; Wobus *et al.*, 2006a).

Equation (2) makes an explicit prediction of the relationship between k_{sn} and uplift rate; which empirical studies have shown both to be linear (Lague & Davy, 2003; Wobus *et al.*, 2006a; Kirby & Whipple, 2012), and nonlinear (Snyder *et al.*, 2003; Cyr *et al.*, 2010). Its form is mediated by bedrock erodibility and the stream power law assumed, which may differ between study areas (e.g. Whittaker, 2012; D’Arcy & Whittaker, 2014). Adjustments of channel geometry and sediment cover in response to tectonic forcing (e.g. Sklar & Dietrich, 2001; Finnegan *et al.*, 2005; Wobus *et al.*, 2006b; Whittaker *et al.*, 2007; Attal *et al.*, 2008) may add scatter or hamper the correlation.

Channels that have completely adjusted to the uplift field of a normal fault are expected to have different values of k_{sn} along the strike of the structure as slip rates vary from tip to centre (Densmore *et al.*, 2007; Miller *et al.*, 2012; Papanikolaou *et al.*, 2013). Additionally, hillslope slopes and footwall relief are expected to be greater where slip rates are higher (e.g. Anders & Schlische, 1994) and channels steeper. If slip rates are greater than erosion rates, slopes will continue steepening and relief will continue to grow as fault displacement increases (Mirabella *et al.*, 2004; Cowie *et al.*, 2006), until they reach the critical threshold dictated by each lithology’s bedrock strength (e.g. Schmidt & Montgomery, 1995; Montgomery & Brandon, 2002). After this critical threshold, erosion rates increase non-linearly through landsliding (e.g. Ouimet *et al.*, 2009; DiBiase *et al.*, 2010). Densmore *et al.* (2004) proposed that this non-linearity explains why relief is constant along the footwalls of some long faults (ca. 140 km, and with numerous segments) of the NE Basin and Range: as cumulative fault slip creates greater relief and steeper slopes towards the centres of faults, erosional processes become more effective and impose a geomorphic threshold (e.g. Strak *et al.*, 2011) that limits further relief growth and decouples the topography from the fault displacement. Additionally, fault footwall relief and range width is also limited by the fault dip and thickness of the seismogenic layer (Scholz and Contreras, 1998), the geometry and spacing of neighbouring faults, and the

extent of hangingwall sedimentation (Densmore *et al.*, 2005).

As mentioned above, bedrock channels crossing faults can experience changes in relative base-level as a result of slip rate increases resulting from fault interaction and linkage (Cowie *et al.*, 2006; Whittaker *et al.*, 2007; Attal *et al.*, 2008). In these cases, channels are expected to progressively steepen, incise and adjust to the new boundary conditions (e.g. Snyder *et al.*, 2000; Attal *et al.*, 2008; Fig. 1). These changes typically precede physical linkage along the faults (Hopkins & Dawers, 2015). The boundary between the incised, lower river reach, and the unincised, unadjusted upper reach is marked by a convexity in the long profile, often referred as knickpoint (Fig. 1b, e; e.g. Crosby & Whipple, 2006; Kirby & Whipple, 2012). As incision progresses, knickpoints migrate upstream with a vertical velocity that is a function of the magnitude of the perturbation experienced (Niemann *et al.*, 2001; Attal *et al.*, 2008, 2011; Whittaker *et al.*, 2008; Whittaker & Boulton, 2012; Whittaker & Walker, 2015). Because knickpoints propagate upstream at analytically predictable rates, and transient long profiles can retain tectonic information for periods $>10^6$ years (e.g. Snyder *et al.*, 2000; Whittaker *et al.*, 2008; Attal *et al.*, 2011), they can be used to extract information about past changes in tectonic boundary conditions (Commins *et al.*, 2005; Wobus *et al.*, 2006a; Boulton & Whittaker, 2009; Miller *et al.*, 2012; Whittaker & Walker, 2015). Hillslope gradients would also adjust to spatial and temporal changes in channel steepness and incision (e.g. Whipple & Tucker, 1999, 2002; Wobus *et al.*, 2006a, b; Kirby & Whipple, 2012), if they have not yet reached their strength-limited threshold.

By combining transient stream profile analysis with normal fault interaction theory, Commins *et al.* (2005) reconstructed the timing of normal fault profile re-adjustment in Utah and the associated magnitude of slip rate change. Similarly, Hopkins & Dawers (2015) studied how channel morphology changes through previously identified stages of fault interaction and linkage. Boulton & Whittaker (2009), and more recently Whittaker & Walker (2015) estimated the time of fault linkage and current throw rates in tectonically active areas of Turkey and Greece by comparing knickpoint heights upstream of faults and k_{sn} values upstream and downstream of knickpoints. Nevertheless, the integrated response of channels and landscapes as normal faults grow and link remains relatively under-researched, by comparison to the numerous studies that link river long profiles to base level changes in general (c.f. Kirby & Whipple, 2012). In particular, we still lack empirical data of river response to active faulting collected systematically along the strike of faults whose slip rates and fault throws are well-constrained, especially for cases in which rock strength-limited thresholds have not yet been reached. Additionally, there has been little work that has attempted to reconcile geomorphic inferences of base-level change with predictions from fault growth and interaction theory. Here, we present new data

to address these challenges, using case studies of normal faults in the Southern Apennines of Italy.

GEOLOGICAL SETTING

The Apennines are a NE verging fold-and-thrust belt generated during the Alpine orogeny as a result of the collision between the African and Eurasian plates (e.g. Pantosti & Valensise, 1990). Since the Pliocene much of the orogenic system has been subjected to back-arc extension (Hippolyte *et al.*, 1994; Papanikolaou & Roberts, 2007; Patacca & Scandone, 2007), attributed to the roll-back of the African plate under the Eurasian plate (e.g. Cinque *et al.*, 1993). In the Southern Apennines, extension accommodates $2\text{--}5\text{ mm year}^{-1}$ of horizontal deformation (e.g. Ferranti *et al.*, 2014). Extensional tectonics has created a large array of NW-SE striking normal faults along the axis of the Apenninic orogen, which overprint the previous compressional structures (Amato & Montone, 1997; Roberts & Michetti, 2004; Papanikolaou & Roberts, 2007). In most cases, these normal faults have attained lengths of $>30\text{ km}$ and displacements of $>1000\text{ m}$, and have generated substantial hangingwall basins (Cinque *et al.*, 1993, 2000; Maschio *et al.*, 2005; Barchi *et al.*, 2006; Papanikolaou & Roberts, 2007). These structures are associated with magnitude 5.5–7.0 earthquakes (Pantosti & Valensise, 1990; Amato & Montone, 1997; Roberts *et al.*, 2004; Villani & Pierdominici, 2010).

We have selected three normal faults in the Campanian-Lucanian sector of the Southern Apennines because they have numerous published constraints regarding their fault geometries and activity, which we evaluate and reconcile in this study: the Vallo di Diano (VDF), East Agri (EAF) and Monti della Maddalena faults (MMF) (Fig. 2). Located in the centre of the Southern Apennines fault array, they bound the two biggest hangingwall basins in the area: the Vallo di Diano (175 km^2) and the Val d'Agri basins (120 km^2). They dip *ca.* $45\text{--}60^\circ$, based on field and seismic data (Maschio *et al.*, 2005; Barchi *et al.*, 2006; Papanikolaou & Roberts, 2007; Amicucci *et al.*, 2008), and their motion is almost purely dip-slip (Papanikolaou & Roberts, 2007). These faults displace a range of Mesozoic and Cenozoic lithologies (Fig. 2b), including platform carbonates thrust during the compressional phase, and Tertiary siliciclastic sediments (flysch units) deposited in the former foredeep of the Apenninic orogen.

Thrusting in the study area had ceased by the Early to Mid Pliocene (Cinque *et al.*, 1993; Hippolyte *et al.*, 1995; Ferranti & Oldow, 2005), because there are *ca.* 3.7 Ma clastic, undeformed deposits which unconformably drape the thrust sheets (Patacca & Scandone, 2007). The presence of Upper Pliocene – Lower Pleistocene sediments in the normal fault hangingwall basins suggest extension in the Southern Apennines started 1.8–3.6 Ma (Oldow *et al.*, 1993; Ferranti & Oldow, 2005; Barchi *et al.*, 2006; Papanikolaou & Roberts, 2007; Bruno *et al.*, 2013). The

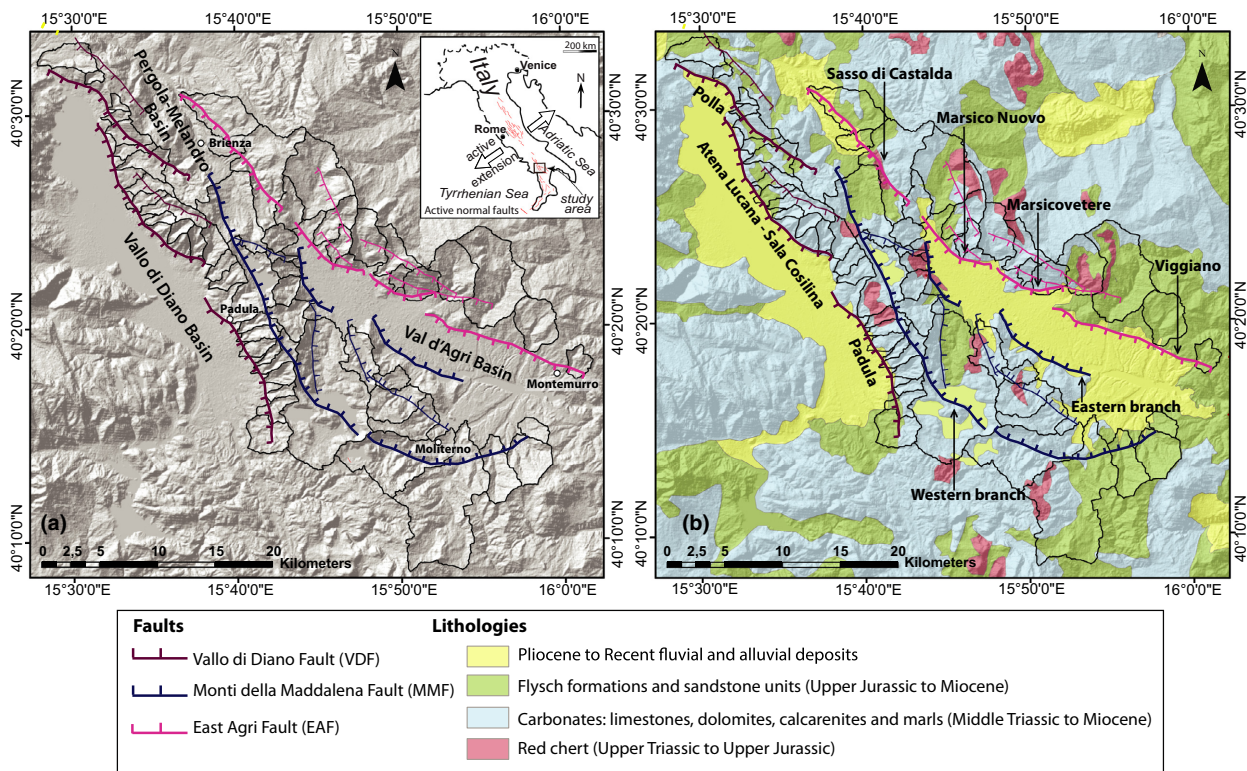


Fig. 2. (a) Hillshade image showing a simplified map of the Vallo di Diano (VDF), Monti della Maddalena (MMF) and East Agri (EAF) faults, with the main fault strands in bold. Footwall catchments along the faults are delimited with black, bold lines. Inset image shows the location of the study area within Italy and the Apennines fault array. (b) Simplified lithological map, with the main basin-bounding fault segments labelled.

oldest dated basin sediments in our study area are Lower-Middle Pleistocene deposits (0.7 ± 0.2 Ma, from boreholes by Santangelo, 1991; and Giano *et al.*, 2014) in the Vallo di Diano basin, and inferred Lower Pleistocene slope deposits in the Val d’Agri basin (Giano, 2011). Nevertheless, seismic imaging in these basins reveals syn-tectonic sequences that are *ca.* 2–4 times thicker than borehole depths, so an Upper Pliocene–Early Pleistocene fault initiation time has been suggested (Barchi *et al.*, 2006; Amicucci *et al.*, 2008; Bruno *et al.*, 2013). For the MMF, a younger, Middle to Late Pleistocene fault initiation age of *ca.* 0.18–0.75-Ma has been proposed, based on the displacement of *ca.* 0.75 Ma surfaces and “inmature morphology” (Maschio *et al.*, 2005), the geometry of alluvial fan deposits on the SE end of the Val d’Agri basin (Zembo *et al.*, 2009, 2012), and palaeoseismological back-stripping calculations (Improta *et al.*, 2010).

For the VDF, Villani & Pierdominici (2010) produced a minimum total throw profile by summing the footwall relief along strike to the bedrock depth in the basin, imaged by 12 ENI-acquired seismic lines, and outlined in an isobaths map (Amicucci *et al.*, 2008). Values for the Polla segment (Fig. 2) were extracted by Villani & Pierdominici from estimates published by Spina *et al.* (2008) and Cello *et al.* (2003) based on geological markers. Additionally, Barchi *et al.* (2006) and Bruno *et al.* (2013) published seismic reflection profiles imaging the hangingwall basin deposits and the bedrock below them, which is up

to *ca.* 1000 m below the basin base level. Papanikolaou & Roberts (2007) also published estimates of total geological throw for the VDF and EAF, based on the offsets of mapped Miocene (on the VDF) and Triassic–Jurassic units (on the EAF). For both sides of the Val d’Agri basin, minimum hangingwall deposits thickness (i.e. minimum bedrock depth below the basin) of up to *ca.* 600 m were imaged on six electrical resistivity tomography (ERT) profiles (Colella *et al.*, 2004), and a geological cross-section based on outcrops along incised alluvial fans (Zembo *et al.*, 2009). Two seismic lines (Barchi *et al.*, 2006) also constrain the bedrock depth on the Val d’Agri basin. Along the MMF footwall there is one published throw constraint, based on the displacement of a Miocene–Pliocene thrust fault (Maschio *et al.*, 2005; Improta *et al.*, 2010).

There are also diverse published constraints on the slip rates of these faults. On the VDF, three throw rate values have been derived by Papanikolaou & Roberts (2007) from bedrock fault scarps that are assumed to be post-glacial. Villani & Pierdominici (2010) obtained a throw rate estimate from scarps on dated alluvial fan deposits (*ca.* 3000–2100 years BP), and Cinque *et al.* (2000) estimated a throw rate averaged since *ca.* 0.4–0.6 Ma from offsets of dated basin deposits. The dip-slip component of the displacement rate has also been geodetically estimated (Ferranti *et al.*, 2014). Constraints on throw rates along the EAF have been obtained from fault bedrock scarps that

are assumed to be post-glacial (Benedetti *et al.*, 1998; Papanikolaou & Roberts, 2007) and offsets of Middle Pleistocene to recent geomorphic markers (Cinque *et al.*, 2000). Along the MMF, there are four published sources of throw rate estimates: geodetic data (Ferranti *et al.*, 2014); presumably post-glacial bedrock and soil scarps (Maschio *et al.*, 2005; Improta *et al.*, 2010); and the displacement of late Pleistocene to recent (post-1.2 Ma) erosional surfaces (Schiattarella *et al.*, 2003).

In our results section, we evaluate how these constraints agree in time and space, because many of these measurements have not yet been reconciled with each other and with respect to faulting history. While Papanikolaou & Roberts (2007) studied the evolution of Southern Apennines normal faults, they could not resolve any slip rate increases based on the array-scale resolution of their data. However, they noted that early faulting history is poorly known, and therefore this possibility could not be ruled out. Our combined geomorphic and tectonic analyses shed light on the evolution of these normal faults.

METHODS

Fault traces and lithologies

Fault segments were mapped based on (i) published maps (Maschio *et al.*, 2005; Villani & Pierdominici, 2010; Zembo *et al.*, 2012), (ii) lithological contacts between basement and Quaternary deposits, (iii) fault escarpments identified in the DEM by laterally continuous, high gradient, breaks in topographic slope, and (iv) field observations. Segment boundaries were further identified based on the identification of relay structures, and changes in the strike of the fault segments, following Cartwright *et al.* (1996), and verified using throw profiles. Geological units were digitized based on the 199 (Potenza), 200 (Tricarico), 210 (Lauria) and 211 (San Arcangelo) 1 : 100 000 Italian Geological Survey maps. Outcropping formations have been grouped into four major lithological classes based on field observations and lithofacies descriptions (Fig. 2b): (i) Pliocene to Recent fluvial and alluvial deposits, (ii) flysch formations and sandstones, (iii) carbonates (limestones, dolomites, calcarenites and marls) and (iv) red chert. Footwall catchments were assigned a dominant lithology when a lithological group covered $\geq 50\%$ of the catchment area; otherwise, they were classified as having “mixed lithologies”.

DEM analysis

Topographic data were acquired from an ASTER digital elevation model (DEM), with a resolution of 27.3×27.3 m, projected in WGS 1984 UTM Zone 33N. A drainage network was obtained using a flow accumulation threshold of 0.37 km^2 (500 pixels), and confirmed against mapped streams on topographic maps. Fifty-seven footwall catchments were extracted upstream

of the mapped fault strands, with drainage areas up to 65 km^2 . Catchments smaller than 1.5 km^2 were excluded, as field observations indicate they are not dominated by fluvial processes.

Swath profiles of the mean, minimum and maximum footwall elevations were constructed across the fault footwalls in ArcMap. Footwall relief profiles were obtained by subtracting the basin base level elevation profile from the footwall elevation profile (e.g. Mirabella *et al.*, 2004). A slope map was derived from the DEM from which we extracted the median slope value for each catchment.

Stream long profiles were extracted for 70 channels draining the fault footwalls, using the Stream Profiler toolbar (Wobus *et al.*, 2006a) in ArcGis and Matlab. To ensure that our extracted drainage networks are representative of the catchments' drainages, if catchments have multiple tributaries that share $< 2/3$ of their total channel length, a stream long profile was extracted for each. For catchments with several tributaries that share at least $2/3$ of their length, only the channel with greater drainage area was extracted. A reference concavity of 0.45 was used to calculate k_{sn} values (e.g. Wobus *et al.*, 2006a; Cyr *et al.*, 2010). Knickpoints (sensu Whittaker & Boulton, 2012) were identified in the stream long profiles and gradient-distance plots, and positioned where the rate of change in the channel gradient was greatest. As this study focuses on landscape response to faulting, knickpoints that were obviously coincident with mapped lithological boundaries were excluded from our analysis. Similarly, only ‘slope-break’ knickpoints (c.f. Kirby & Whipple, 2012; their Fig. 4), that bound a lower section of the channel recording at least a 10% increase in channel steepness were included, as ‘vertical-step’ knickpoints – unassociated with changes in steepness index – are typically related to changes in bedrock erodibility (Kirby & Whipple, 2012). For completeness, we have included in the supplementary material the long profiles of all the analysed channels, with the identified slope-break knickpoints, and the modelled fits of k_{sn} for the channel sections above and below the knickpoints. Following Whittaker & Walker (2015), the vertical heights of knickpoints were measured from the elevation of the mapped main fault trace that bounds the footwall catchments.

Total throw profiles and throw rate constraints

Throw and throw rates are often used in geomorphic studies because they can be measured independently of fault dip and because rivers are most sensitive to the vertical uplift rate (e.g. Whittaker *et al.*, 2007). We built minimum total throw (vertical component of the net displacement) profiles using: (i) published total geological throw estimates by Papanikolaou & Roberts (2007), Maschio *et al.* (2005) and Improta *et al.* (2010); (ii) seven new measurements of geological throw along the W-strand of the MMF fault, derived from the offset of mapped (1 : 100 000 Italian Geological Survey maps, references

above) Cretaceous to Miocene bedrock units (see supplementary material); and (iii) estimates of the minimum geological throw, given by the minimum bedrock depth in the hangingwall basins, measured from the basin base level (derived from published estimates by Colella *et al.*, 2004; Barchi *et al.*, 2006; Amicucci *et al.*, 2008; Zembo *et al.*, 2009 and Bruno *et al.*, 2013; see Geological Setting) and the sum of the footwall relief measured from the basin base level. The latter approach has been validated in faults with dominantly dip-slip movement (e.g. Mirabella *et al.*, 2004; Villani and Pierdominici, 2010), but because footwall erosion is neglected, it provides only minimum estimates of the total throw accumulated throughout faulting history. Our calculations of minimum total throws, together with the published constraints that we use, can be found in tables in the supplementary material.

Constraints are plotted at the along-strike positions where they were obtained. If these were not provided (e.g. Cinque *et al.*, 2000), we consider these constraints as a minimum estimates and plot them at the centre of the faults, with generous error bars. Total throw profiles are built by interpolating all the available constraints along the fault strike. In the MMF, we use the mean of Maschio *et al.* (2005) and Improta *et al.* (2010) throw and throw rate estimates because they were acquired from the same scarps. We assume that throw decays to zero at the tips of the mapped faults, as observed by Papanikolaou & Roberts (2007) and Villani & Pierdominici (2010). We propagated the error estimates of the published constraints, or if not provided, we applied a conservative $\pm 20\%$ error, in line with previous works on normal faults (e.g. Densmore *et al.*, 2004; Papanikolaou & Roberts, 2007).

Bedrock fault scarps along the Apennines normal faults have been used by a number of authors to estimate fault throw rates; they are generally assumed to be post-glacial, because it is considered unlikely that they could have been preserved under periglacial conditions (Roberts & Michetti, 2004; Papanikolaou & Roberts, 2007; Faure-Walker *et al.*, 2009). This assumption is supported by exposure dating (^{36}Cl) of the fault scarp in the Magnola fault (Central Apennines) by Palumbo *et al.* (2004) and Schlagenhauf *et al.* (2011). Due to the uncertainty on the last glacial maximum age on the Southern Apennines (15 ± 3 ka, Roberts & Michetti, 2004; Faure-Walker *et al.*, 2009), throw rate constraints could have errors up to $\pm 20\%$. In our analysis, we assume an age of 18 ka for consistency with published data sets (Roberts & Michetti, 2004; Papanikolaou & Roberts, 2007), but we propagate errors accordingly. Most throw rate constraints used are recent (post *ca.* 3 ka, or geodetic measurements) or post-glacial, so we refer to them generically as post-18 ka throw rates. The only exceptions are rates from Cinque *et al.* (2000), and Schiattarella *et al.* (2003), which represent time-averaged throw rates over longer timescales. Data from Cinque *et al.* (2000) are based on the displacement of deposits attributed to the Middle Pleistocene, while the data of Schiattarella *et al.* (2003) are based on

the displacement of an erosional surface supposed by the authors to be *ca.* 1.2 Ma. We plot the throw rate constraints on the along strike position where they were measured.

RESULTS

Here, we characterize the tectonic activity of the VDF, EAF, and MMF normal faults (Fig. 2), and evaluate their effects on catchment geomorphology and river long profiles, for a range of lithologies. Based on published geological maps (see Methods), we observe that flysch and sandstone formations outcrop mostly in the E-SE and NW parts of the EAF and MMF footwalls, whereas the central areas of these footwall blocks are dominated by carbonate formations and some red chert (Fig. 2b). Competent limestones and dolomites form the VDF footwall, alongside minor outcrops of red chert and flysch. Pliocene to Recent deposits infill the hangingwall and perched basins.

Fault traces, footwall catchments, and relief

We estimate the VDF has a total length of *ca.* 38 km (*ca.* 2 km longer than proposed by Villani & Pierdominici, 2010). It bounds 26 catchments, with areas 1.5–19 km² (mean: *ca.* 5 km²) (Fig. 2). The fault has three main SW-dipping basin-bounding segments, named by Villani & Pierdominici (2010) from north to south: Polla, Atena Lucana–Sala Cosilina (AL-SC), and Padula segments (Fig. 2b). The northern and central segments overlap for about 9 km, creating a relay ramp. Two minor strands are sub-parallel to the Polla and AL-SC segments, the northernmost referred often as the “Caggiano fault” (e.g. Cello *et al.*, 2003; Soliva *et al.*, 2008; Spina *et al.*, 2008).

We find that the EAF has a length of *ca.* 43 km, 10 km more than previously reported (Benedetti *et al.*, 1998; Cello *et al.*, 2003; Giano, 2011), in agreement with recent work by Giocoli *et al.* (2015) that indicates that the fault extends south up to the town of Montemurro (Fig. 2a). It bounds 15 catchments with areas 2.4–32 km² (mean: *ca.* 13 km²); the northern three drain into the Pergola–Melandro basin, the rest into the Val d’Agri basin (Fig. 2a). The fault has four main SW-dipping segments, which we named, from north to south: Sasso di Castalda, Marsico Nuovo, Marsicovetere and the Viggiano segments (Fig. 2b). The two central segments have two minor sub-parallel strands that have generated bedrock scarps in the catchments.

The MMF fault is mapped along *ca.* 36 km, further south than published maps, based on: (i) the presence of thick (>150 m, Zembo *et al.*, 2012) Pleistocene to recent alluvial fan deposits downstream of the southernmost catchments, which suggests that there might be a buried normal fault on this area, and (ii) recent microseismicity surveys, which have reported a cluster of low-magnitude

earthquakes ($M < 2.7$) on this region (e.g. Valoroso *et al.*, 2009). In contrast with Maschio *et al.* (2005) and Zembo *et al.* (2012), we do not find conclusive evidence for the fault extending N into the Pergola-Melandro basin (Fig. 2). We have extracted 16 footwall catchments with areas 2–65 km² (mean: 17 km²), all but the northernmost draining into the Val d'Agri basin. Several perched basins lie along the footwall, infilled with Quaternary deposits (Fig. 2b). The fault has two main parallel strands dipping towards the NE: a western one that runs close to the drainage divide with the VDF catchments, and an eastern one bounding the SW side of the Val d'Agri basin; as well as some minor strands that create several relay zones between them (Fig. 2).

Swath profiles (Fig. 3) show maximum elevations of ca. 1400–1600 m for the three footwall blocks, and mean elevations of ca. 800–1400 m. In the VDF and EAF, footwall relief varies between 200 and 900 m, reaching the maximum at the fault centres and decaying towards the fault tips (Fig. 3a–b). The footwall relief mirrors the mapped fault segments (Fig. 2b), with minimum values at the segment boundaries. However, for the MMF footwall (Fig. 3c) fault segments cannot be distinguished.

Fault throws and post-18 ka throw rates

Vallo di Diano Fault

We have recalculated the VDF total throw profile published by Villani & Pierdominici (2010), by: (i) summing the throws in relay zones and overlapping segments (c.f. Dawers & Anders, 1995), in contrast with Villani & Pierdominici, who only aggregated the displacement of two strands where two discrete measurements overlapped along strike (Fig. 4a); and (ii) complementing this profile with total throw estimates published by Papanikolaou & Roberts (2007), and those that we derive from the hangingwall subsidence data by Barchi *et al.* (2006) and Amicucci *et al.* (2008) (see supplementary material). At the fault centre, these estimates agree well with Villani & Pierdominici's profile. However, our inferred profile in the northern sector of the Polla segment (dashed, Fig. 4a) differs from theirs, because we consider the Caggiano fault as a branch of the VDF (c.f. Soliva *et al.*, 2008; Spina *et al.*, 2008; Papanikolaou & Roberts, 2007). In the northern section of the Padula segment, our minimum throw estimates derived from seismic profiles by Amicucci *et al.* (2008) and Bruno *et al.* (2013) suggest that total throw is lower than that inferred by Villani & Pierdominici (2010), so we modify our profile accordingly (dashed, Fig. 4a).

Total throw (Fig. 4a) displays three maxima at the centres of the three mapped fault segments (Fig. 2), separated by a local minimum that corresponds to the relay zone between the Polla and the AL-SC segments and a southern minimum between the AL-SC and Padula segments. Total throw is highest at the centre of the central

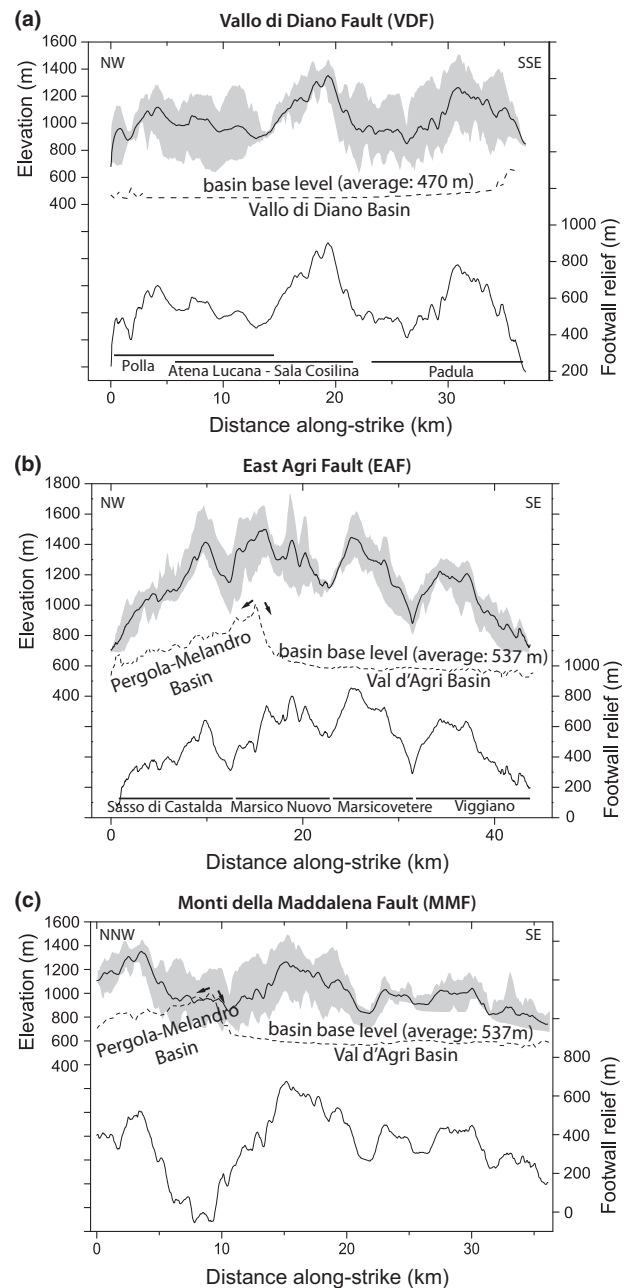


Fig. 3. Swath profiles of the footwall blocks of the VDF (a), EAF (b) and MMF (c), taken along the fault strikes. Footwall relief profiles were obtained by subtracting the basin base level from the mean elevations of the swaths (black, bold line).

segment, reaching values of ca. 2000 m. Footwall relief apparently mirrors the mapped geological fault segment boundaries: for instance where the Padula and Sala Cosilina segments meet there is marked (but non zero) relief minimum. Because geological throw estimates (Papanikolaou & Roberts, 2007), and the minimum throw estimates based on the sum of the footwall relief and the bedrock depth on the hangingwall (Villani & Pierdominici, 2010; our estimates using seismic profiles from Barchi *et al.*, 2006; Amicucci *et al.*, 2008; Bruno *et al.*, 2013) are generally in close agreement, we hypothesize that erosion of the

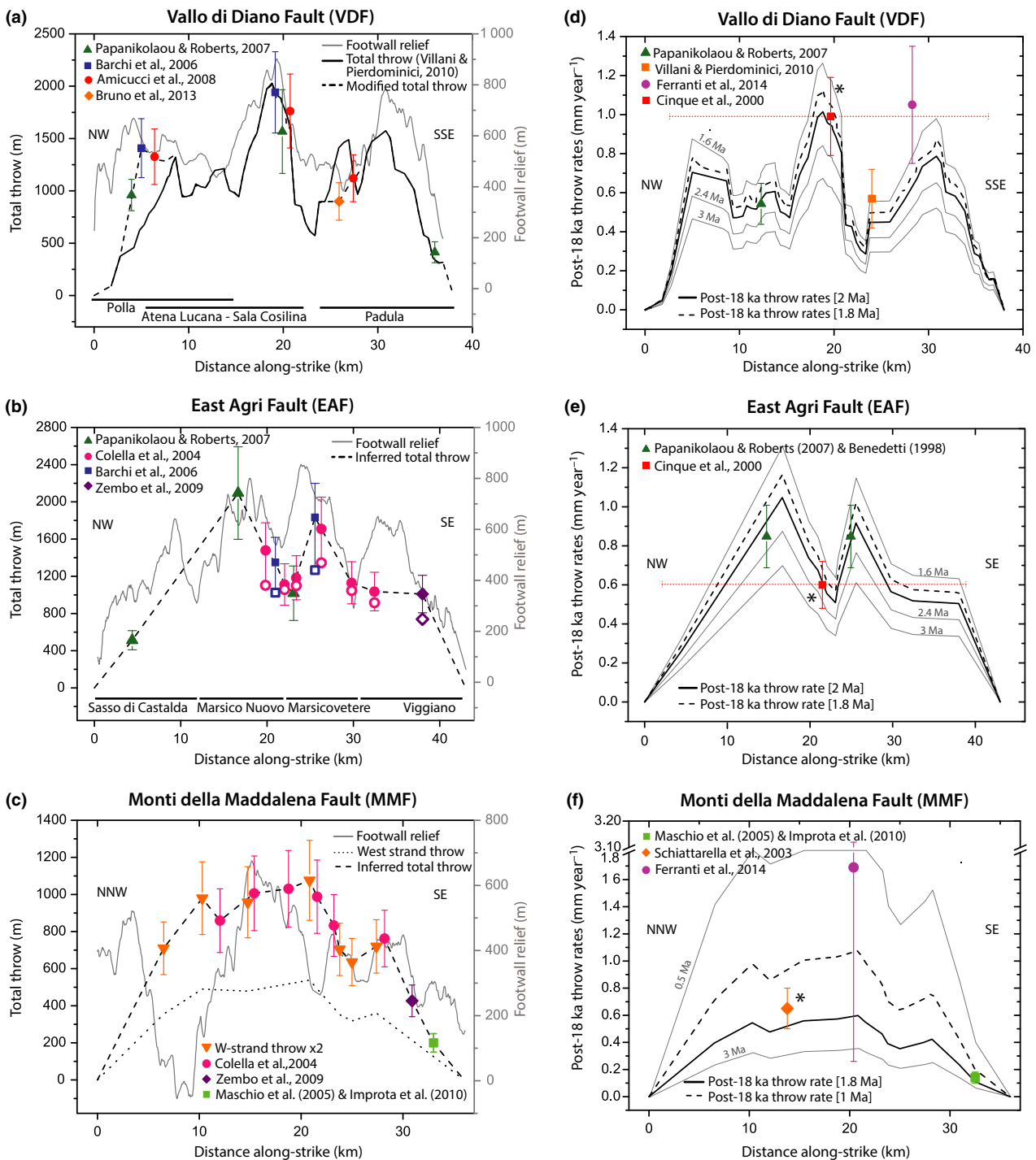


Fig. 4. Total throw (a–c) and post-18 ka throw rate (d–f) profiles along fault strikes, built from the constraints showed here. We also show throw rate profiles derived from different fault initiation times for comparison. An asterisk indicates that the data point represents throw rates averaged over a longer time period than 18 ka (see text). The x-error bars from the Cinque *et al.* (2000) constraints indicate the uncertainty in the position along strike from where they derived their data.

footwall block has not been enough to reduce its relief significantly. Otherwise, our minimum throw estimates that use footwall relief as input, would be significantly lower than geological throw estimates. In this case, based on the depth of the carbonatic bedrock on the hangingwall basin (up to *ca.* 1000 m across the central area of the basin), and the footwall relief along the fault (up to *ca.* 900 m in the fault centre), we can infer that fault total throw is almost

equally divided (~1 : 1) between the footwall uplift and the hangingwall subsidence.

East Agri Fault

To build the EAF profile (Fig. 4b), we integrated: (i) Papanikolaou & Roberts' (2007) geological throw estimates; and (ii) newly derived minimum throw

estimates, from the minimum bedrock depth on the hangingwall and the footwall relief. For all these new estimates, the minimum footwall throw values were higher than the minimum hangingwall subsidence estimates. For the footwall relief (i.e. footwall elevation minus the basin base level) to be greater than the hangingwall subsidence (i.e. bedrock depth below the hangingwall sediments), the basin would need to be severely underfilled, which is not the case (e.g. Zembo *et al.*, 2009). We contend that the published minimum hangingwall subsidence values are lower than our obtained footwall relief values because constraints from Colella *et al.* (2004) and Zembo *et al.* (2009) only provide minimum bedrock depth estimates, and Barchi *et al.* (2006) have relatively large uncertainties in their depth/velocity conversion model. Therefore, we rectify our estimates of minimum throw assuming a minimum 1 : 1 partitioning between the hangingwall subsidence and footwall throw, as observed on the VDF. This is also the minimum ratio suggested by theoretical considerations and fault geometries datasets (e.g. Anders *et al.*, 1993; Stein *et al.*, 1988; Anders & Schlische, 1994; King *et al.*, 1988). This correction only produced substantial changes to the throw values for four data points, and we extend our range of error to include the uncorrected data point (Fig. 4b).

The fault has four footwall relief maxima, which correlate with the centres of the geologically mapped fault segments, and two derived throw maxima: one at *ca.* 17 km, corresponding to the centre of the Marsico Nuovo segment, with *ca.* 1800 m of throw; and one at *ca.* 27 km along strike, the centre of the Marsicovetere segment, with *ca.* 2100 m of throw. They are separated by a minimum where throw drops to *ca.* 1000 m. In contrast with the VDF, there are far fewer constraints in the northern and southern distal segments of the fault, which reduces the resolution of the throw profile in these sectors.

Monti della Maddalena Fault

The MMF is composed of two main sub-parallel fault strands (Fig. 2). We have estimated the geological throw across the western strand (dotted line in Fig. 4c) from the offsets of geological markers across seven geological cross-sections (in the supplementary information). However, total throw is partitioned between the two subparallel strands: a western one running along the footwall, and an eastern one bounding the hangingwall basin, whose displacement is mostly buried under the hangingwall sediments. Hence, in order to convert these western-strand throw constraints to total throw estimates, we follow two approaches. Firstly, we assume an equal throw partitioning between the two strands, and plot the summed values where our new throw estimates have been obtained (orange triangles, Fig. 4c). Secondly, we add the western strand geological throws (from dotted profile) to the minimum hangingwall subsidence values estimated from

Colella *et al.* (2004) and Zembo *et al.* (2009) (pink circles, Fig. 4c). Bedrock in the basin is at shallower depths than in the EAF side of the fault, so it can be imaged by Colella *et al.*'s (2004) ERT profiles (which image to depths up to *ca.* 600 m). As the data two sets give similar results, we combine them to produce a total throw profile (dashed, Fig. 4c).

The total throw profile resembles that expected for normal faults (e.g. Cowie, 1998; McLeod *et al.*, 2000; Cowie & Roberts, 2001), with a maximum throw of *ca.* 1100 m that decays towards the tips (Fig. 4c). Throw is poorly reflected by the footwall relief, likely because the MMF footwall is a horst also bounded by the VDF (Fig. 2), which is thought to have a longer faulting history and higher throw rates (see Geological Setting and Fig. 4d, f).

Post-18 ka throw rate profiles

Estimates of time-averaged throw rate along strike since fault initiation were constructed by backstripping the total throw profiles using the documented post-18 ka throw rates: i.e. the total throw profiles presented above were divided by possible fault initiation ages using 0.2 Ma increments, and the results which best fitted the post-18 ka constraints along strike were selected (Fig. 4d–f). For the VDF and EAF we select the mean values between the two most likely profiles differing by 0.2 Ma (Fig. 4d–e), with an error envelope of $\pm 10\%$ from each of these profiles.

The time-averaged throw rate profiles that best match the independent post-18 ka rates for these two faults imply minimum fault initiation ages of *ca.* 1.8–2 Ma, which gives a range of throw rates along strike between 0 and *ca.* 1 mm year⁻¹ for both faults (Fig. 4d–e). Fault initiation times younger than this require, to produce the observed minimum throw, greater time-averaged throw rates than those documented by most of the constraints for the last *ca.* 18 ka. The geodetically estimated throw rate value from Ferranti *et al.* (2014) on the VDF only agrees with the 1.8 Ma fault initiation profile at their lower error limit, but these constraints are derived from short-lived geodetic surveys whose long-term applicability is uncertain. For the MMF, post-18 ka throw rate constraints fall between a wider range of throw rate profiles produced using minimum fault initiation ages of 1 and 1.8 Ma (Fig. 4f), so we include this range in the error envelope for the MMF. Geodetic measurements of vertical displacement from Ferranti *et al.* (2014) have a very large uncertainty, but include the suggested range of values. A fault initiation age of 1.4 Ma is the mean fit to the post 18 ka data and would imply time-average throw rates of 0–0.7 mm year⁻¹ since this period.

We emphasize that because in some cases we have summed hangingwall subsidence to measurements of footwall relief, these total throw, throw rate, and fault initiation times must be considered minimum estimates. However, independently derived geological throw

constraints from Papanikolaou & Roberts (2007) are very close to our estimates, giving us confidence that our values are reasonable. Finally, we stress that the fault initiation times used here are those required to convert total throw profiles into time-averaged throw rate profiles that best match the post-18 ka constraints. However, fault interaction and linkage would lead to a throw rate increase over time (Fig. 1); if this has taken place, then the real fault initiation ages would also be older than described here. Papanikolaou & Roberts (2007) found inconclusive evidence for significant throw rate increases in this area but could not reject the possibility. We use these throw rate estimates below, but we return to this issue in the discussion, after examining the geomorphological indicators of fault activity.

Catchment response to tectonics and lithology

The slope map (Fig. 5a) shows that steep slopes ($>20^\circ$) are preferentially distributed in narrow bands along and/or above the fault traces, especially in the centres of the segments, and along some footwall channels, reflecting incision. Additionally, relay zones between segments can be identified as bands of gentler gradients crossing several catchments (e.g. between the Polla and the AL-SC segment in the VDF; and between the W and E strands of the MMF). Thus, we hypothesize that catchment slopes are tectonically controlled, either directly, via fault-related base-level change close to fault planes; or indirectly, triggering channel incision that in turn steepens the hillslopes at the valley sides of the channels.

Figure 5b shows the main channels draining the footwall catchments, coloured according to their k_{sn} $m^{0.9}$ values (also presented on Table 1). Channels are steeper in

the centres of the faults and segments, and progressively less steep towards the fault and segment tips. Catchments along the MMF are an exception: many channels run parallel to the fault segments along wide relay zones instead of across them, and hence experience lower cumulative uplift because they are not crossing both main fault strands.

We contrast and compare channel and catchment-averaged k_{sn} values, median slopes (S_{50} , also on Table 1) and throw and throw rates along faults strike in Fig. 6. For the VDF (Fig. 6a), there is a good correlation between catchment slopes, channel slopes, and fault activity. Hill-slopes and channels are steeper in the centres of the fault segments where throw and throw rates are higher, and decay markedly towards their tips and segment boundaries. The exception is the relay ramp between the Polla and AL-SC segments (*ca.* 10 km along strike), where hillslopes and channel metrics do not match the throw rate profile, because the latter represents the summed profile of both segments, while the relay ramp channels only drain across the AL-SC segment (see Fig. 5b).

In the EAF, hillslope, channel steepness and fault throw and throw rates also correlate well, with lower values at the fault tips that become progressively greater towards the fault centre (Fig. 6b). The S_{50} and k_{sn} profiles define a clear single-humped shape in contrast to the post-18 ka throw rate profile, which has two peaks separated by a marked throw low. Given the large density of independent constraints that we have in this sector of the fault (Fig. 4b), which include measured geological throw from a bedrock horizon (Papanikolaou & Roberts, 2007), it is most probable that a real throw deficit, rather than simply a relief deficit, exists in this area. Therefore, we suggest that a recent throw rate increase may have occurred at the fault centre, to which catchment

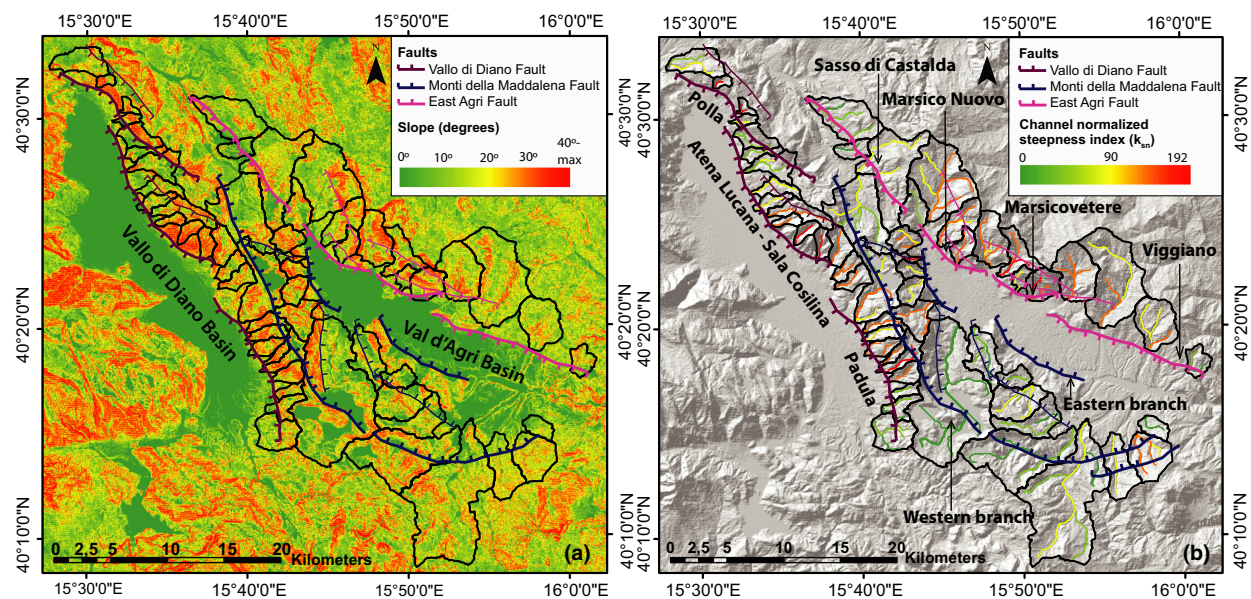


Fig. 5. (a) Slope map of the study area (b) Hillshade map showing the channels draining the footwall catchments, coloured according to their k_{sn} value.

Table 1. Median Slope (S_{50}), catchment-averaged whole channel k_{sn} , catchment-averaged k_{sr} of the sections above and below knickpoints and knickpoint heights from fault, for all studied catchments (catchment numbers in Fig. 6). Stream long profiles for the Vallo di Diano and East Agri faults can be found in the supplementary material.

| Fault | Fault segment | Catchment number | S_{50} , median slope (degrees) | Whole channel* k_{sn} ($m^{0.9}$), $\theta = 0.45$ | k_{sn}^1 , lowest reach | k_{sn}^2 , upper or middle reach | k_{sn}^3 , upper reach | k_{sn}^1 / k_{sn}^2 | Average ratio of segment | k_{sn}^2 / k_{sn}^3 | Average ratio of segment | Knickpoint height from fault (m), lowest or single | Knickpoint height from fault (m), upper | |
|------------------------------|------------------------|------------------|-----------------------------------|--|---------------------------|------------------------------------|--------------------------|-----------------------|--------------------------|-----------------------|--------------------------|--|---|-----|
| Vallo di Diano Fault | Polla | 1 | 11.6 | 64 ± 13 | 87 ± 12 | 63 ± 9 | 46 ± 12 | 1.4 | 1.7 | 1.4 | 1.4 | 170 ± 48 | 281 ± 71 | |
| | | 2 | 21.3 | 131 | — | — | — | — | — | — | — | — | — | |
| | | 3 | 19.9 | 131 ± 3 | 184 ± 17 | 85 ± 24 | — | 2.2 | — | — | — | 198 ± 13 | — | |
| | | 4 | 18.0 | 76 | 128 | 86 | — | 1.5 | — | — | — | 189 | — | |
| | | 5 | 15.4 | 60 ± 2 | — | — | — | — | — | — | — | — | — | |
| | | 6 | 11.9 | 63 | — | — | — | — | — | 2.5 | — | — | — | |
| | | 7 | 11.8 | 69 ± 3 | 130 | 80 ± 17 | 17 | 1.6 | — | — | 4.7 | — | 159 | 369 |
| | | 8 | 13.3 | 69 | 92 | 56 | 32 | 1.6 | — | — | 1.8 | — | 287 | 465 |
| | | 9 | 14.1 | 71 | 89 | 42 | — | 2.1 | — | — | — | — | 270 | — |
| | | 10 | 18.6 | 105 | 150 | 64 | 43 | 2.3 | — | — | 1.5 | — | 467 | 660 |
| Atena Lucana – Sala Cosilina | Lucana – Sala Cosilina | 11 | 24.1 | 95 | 104 | 88 | 35 | 1.2 | — | 2.5 | — | 248 | 337 | |
| | | 12 | 27.3 | 133 | 223 | 112 | 53 | 2.0 | — | 2.1 | — | 332 | 608 | |
| | | 13 | 27.2 | 162 | 162 | 86 | — | 1.9 | — | — | — | 543 | — | |
| | | 14 | 20.2 | 96 | 168 | 31 | — | 5.4 | — | — | — | 494 | — | |
| | | 15 | 15.4 | 96 ± 1 | 158 ± 3 | 52 ± 5 | — | 3.0 | — | — | — | 364 ± 20 | — | |
| | | 16 | 17.3 | 99 | 122 | 32 | — | 3.8 | — | — | — | 446 | — | |
| | | 17 | 15.3 | 81 ± 30 | 189 | 19 ± 18 | — | 9.9 | 3.3 | — | — | 476 ± 97 | — | |
| | | 18 | 21.4 | 104 | 120 | 43 | — | 2.8 | — | — | — | 590 | — | |
| | | 19 | 20.2 | 123 | 139 | 96 | — | 1.4 | — | — | — | 555 | — | |
| | | 20 | 19.3 | 105 ± 11 | 126 ± 11 | 90 ± 9 | — | 1.4 | — | — | — | 263 | — | |
| Padula | Padula | 21 | 20.2 | 120 | 147 | 82 | — | 1.8 | — | — | — | 369 | — | |
| | | 22 | 15.4 | 156 | 202 | 46 | — | 4.4 | — | — | — | 248 | — | |
| | | 23 | 20.9 | 111 | — | — | — | — | — | — | — | — | — | |
| | | 24 | 17.1 | 68 | 74 | 64 | — | — | — | — | — | 147 | — | |
| | | 25 | 13.3 | 53 ± 12 | 73 ± 33 | 21 ± 1 | — | 1.2 | — | — | — | 215 ± 10 | — | |
| | | 26 | 13.6 | 55 ± 14 | — | — | — | 3.5 | — | — | — | — | — | |

(continued)

Table 1 (continued)

| Fault | Fault segment | Catchment number | S ₅₀ , median slope (degrees) | Whole channel* k _{sn} (m ^{0.9}), θ = 0.45 | k _{sn} ¹ , lowest reach | k _{sn} ² , upper or middle reach | k _{sn} ³ , upper reach | k _{sn} ¹ / k _{sn} ² | Average ratio of segment | k _{sn} ² / k _{sn} ³ | Average ratio of segment | Knickpoint height from lowest or single fault (m), upper | Knickpoint height from fault (m), upper |
|-----------------------------|-------------------|------------------|--|--|---|--|--|---|--------------------------|---|--------------------------|--|---|
| East Agri Fault | Sasso di Castalda | 27 | 10.7 | 54 ± 9 | - | - | - | - | 1.7 | - | - | - | - |
| | | 28 | 8.5 | 18 | - | - | - | - | - | - | - | - | - |
| | | 29 | 13.9 | 77 ± 3 | 115 ± 31 | 69 ± 6 | - | 1.7 | - | - | 151 | - | - |
| | Marsico Nuovo | 30 | 13.8 | 64 | 78 | 70 | 24 | 1.1 | 1.6 | 2.9 | 159.0 | 299 | 299 |
| | | 31 | 13.7 | 85 ± 13 | 141 | 97 ± 19 | 29 ± 8 | 1.5 | - | 3.3 | 170 | 532 ± 114 | 532 ± 114 |
| | | 32 | 16.8 | 104 ± 18 | 109 ± 13 | 43 | - | 2.5 | - | - | 387 | - | - |
| | | 33 | 16.7 | 99 | 105 | 81 | - | 1.3 | - | - | 403 | - | - |
| | Marsico-vetere | 34 | 21.7 | 97 ± 20 | 118 ± 21 | 85 ± 28 | - | 1.4 | 1.8 | - | 300 ± 34 | - | - |
| | | 35 | 16.6 | 141 ± 20 | 170 ± 9 | 51 ± 31 | - | 3.3 | - | - | 573 ± 56 | - | - |
| | | 36 | 16.3 | 79 | - | - | - | 1.1 | - | - | - | - | - |
| | | 37 | 17.7 | 112 ± 18 | 127 ± 21 | 85 ± 3 | - | 1.5 | - | - | 376 ± 57 | - | - |
| | Viggiano | 38 | 15.8 | 101 ± 8 | 146 | 110 ± 5 | 54 ± 4 | 1.3 | 1.8 | 2.0 | 258 | 532 ± 72 | 532 ± 72 |
| | | 39 | 14.5 | 83 ± 9 | 86 ± 13 | 66 ± 1 | - | 1.3 | - | - | 311 ± 86 | - | - |
| | | 40 | 13.9 | 88 ± 12 | 108 ± 6 | 63 ± 14 | - | 1.7 | - | - | 252 ± 85 | - | - |
| | | 41 | 13.3 | 48 ± 11 | 50 | 17 | - | 2.9 | - | - | 111 | - | - |
| Monti della Maddalena Fault | | 42 | 12.9 | 67 ± 31 | - | - | - | - | - | - | - | - | - |
| | | 43 | 23.5 | 101 ± 28 | - | - | - | - | - | - | - | - | - |
| | | 44 | 18.2 | 142 | - | - | - | - | - | - | - | - | - |
| | | 45 | 21.6 | 74 | - | - | - | - | - | - | - | - | - |
| | | 46 | 19.2 | 76 | - | - | - | - | - | - | - | - | - |
| | | 47 | 17.7 | 115 ± 1 | - | - | - | - | - | - | - | - | - |
| | | 48 | 11.1 | 29 ± 8 | - | - | - | - | - | - | - | - | - |
| | | 49 | 11.5 | 53 ± 9 | - | - | - | - | - | - | - | - | - |
| | | 50 | 10.6 | 57 | - | - | - | - | - | - | - | - | - |
| | | 51 | 12.9 | 71 ± 11 | - | - | - | - | - | - | - | - | - |
| | | 52 | 12.8 | 49 ± 5 | - | - | - | - | - | - | - | - | - |
| | | 53 | 14.7 | 43 ± 13 | - | - | - | - | - | - | - | - | - |
| | | 54 | 14.0 | 59 ± 18 | - | - | - | - | - | - | - | - | - |
| | | 55 | 15.7 | 73 | - | - | - | - | - | - | - | - | - |
| | | 56 | 17.0 | 97 ± 14 | - | - | - | - | - | - | - | - | - |
| | | 57 | 8.8 | 41 | - | - | - | - | - | - | - | - | - |

*For catchments that have more than one tributary channel, we present catchment-averaged values for the whole-channel k_{sn}, the k_{sn} sections above and below knickpoints, and the knickpoint heights. The ± errors represent the scatter of values for the different tributaries in the catchments.

AL-SC, Atena Lucana-Sala Cosilina; Sasso, Sasso di Castalda; M. Nuovo, Marsico Nuovo; M. Vetere, Marsicovetere.

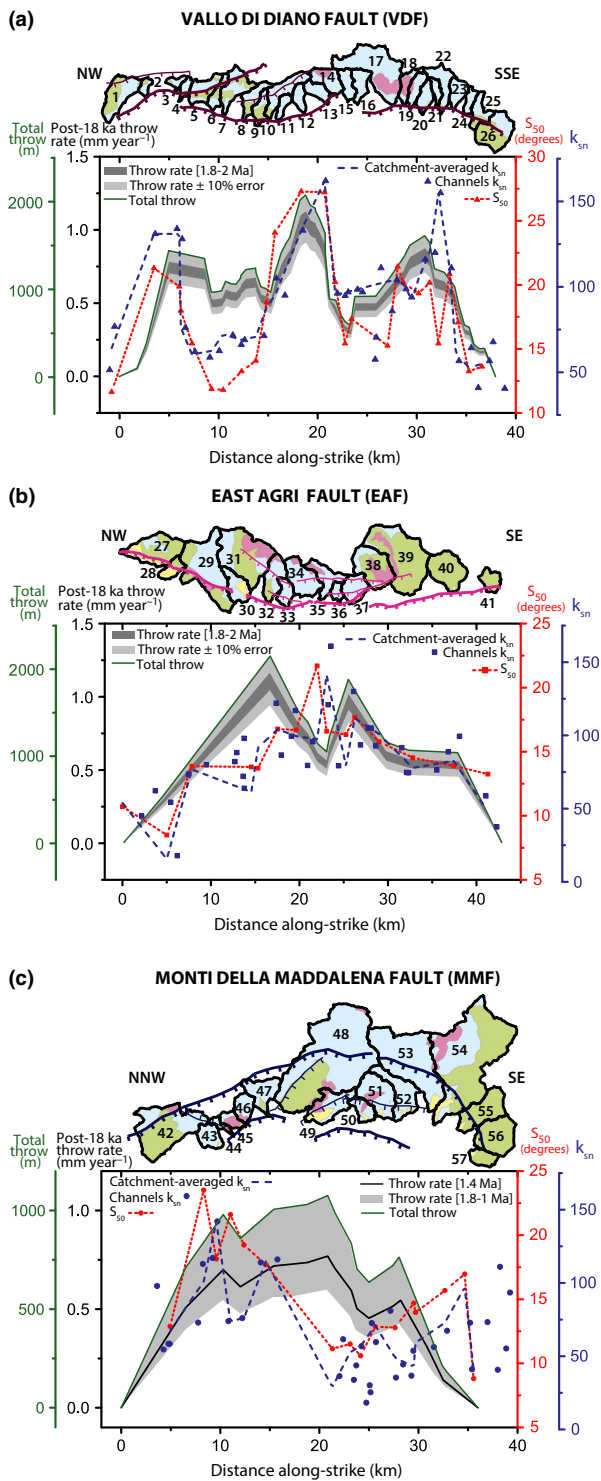


Fig. 6. Along strike distribution of fault total throws, post-18 ka throw rates, S_{50} , and channels and catchment-averaged k_{sn} values. For the VDF (a) and EAF (b), the throw rate values between the two most likely post-18 ka profiles from Fig. 4, are coloured in dark grey, while the range of uncertainty in those estimates is shown in lighter grey. For the MMF (c), the mean value between the likely range of throw rates from Fig. 4 is shown as a bold, black line, and the wider range of uncertainty in lighter grey. Main fault strands, footwall catchments, and the lithologies underlying them are shown above the graphs. The numbering of the catchments corresponds to that used in Table 1.

geomorphology has adjusted, but which has not generated sufficient cumulative throw to remove this deficit (see Discussion). This is unlikely to be captured by Cinque *et al.*'s (2000) published throw rate constraint (red square, Fig. 4e), as it is time-averaged since the Middle Pleistocene and its location along strike is not made precise by the authors.

For the MMF, S_{50} and k_{sn} values correlate well together, but, like relief (Fig. 4c), they do not reflect the inferred post-18 ka throw rate profile (Fig. 6c). We hypothesize that the geomorphology of these catchments does not reflect fault activity well for two important reasons. One is the interaction with the displacement field of the VDF, a faster-slipping and likely older structure that has generated much of the range's relief. The other is the geometry of the fault, which creates multiple wide relay zones through which channels flow, and thus channels experience a tectonic forcing that reflects segment interaction (Hopkins & Dawers, 2015) but not the cumulative throw rate.

Overall, for the VDF and EAF, geomorphology is a good reflection of normal fault activity (Fig. 6a, b), and we exploit this to explore the evolution of these two faults below. We do not observe in Fig. 6a, b a significant lithological modulation in the way these catchments record the active tectonics. Despite the fact that the VDF footwall is dominated by carbonates, and the EAF footwall has a mix of carbonates and flysch sandstones, we observe a similar range of k_{sn} and S_{50} values along both fault systems. The southeastern catchments of the EAF fault have mostly flysch sandstone bedrock, and exhibit similar k_{sn} and S_{50} values to other catchments affected by similar throw rates that are covered by carbonates or mixed lithologies.

Because channels set the boundary condition for hill-slopes, we expect catchment slopes and k_{sn} to correlate. We have observed this in all the faults (Fig. 6a–c), and we test this explicitly in Fig. 7. We find that these

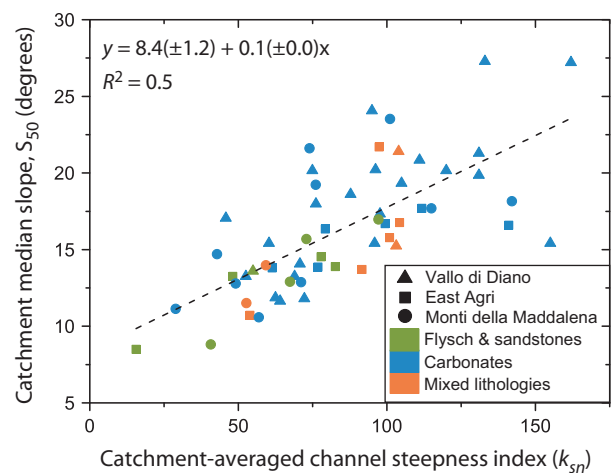


Fig. 7. S_{50} plotted against catchment-averaged k_{sn} values for all footwall catchments of the VDF, EAF and MMF, coloured by their dominant lithology.

geomorphic metrics correlate well ($R^2=0.5$), with catchments getting *ca.* 1° steeper for each 10-point increase in k_{sn} . Therefore, these channels are effectively propagating tectonic signals to the hillslopes. Importantly, all studied lithologies follow the same trend, so we hypothesize that adjustment of hillslopes to channel boundary conditions happens in a similar manner and in a similar timescale for all studied lithologies, which supports our findings of only minor lithological control. The remaining scatter might be explained by footwall uplift and rotation, which would partially influence catchment slopes directly in addition to channel incision; or by different parts of the channels incising at different rates. This last hypothesis would imply that some parts of the catchment, and therefore their slopes, diverge from the catchment-averaged whole channel k_{sn} , which we examine in the Discussion.

Knickpoints and fault interaction

Information about faulting history can be extracted from the presence of knickpoints in the channels. For this analysis we focus on the VDF and EAF because their footwall catchments appear to record fault activity coherently. We include the long profiles of the 70 channels draining the VDF and EAF footwalls in the supplementary material, with the identified knickpoints and modelled k_{sn} values. Catchment maps in Fig. 8 show the distribution of slope-break knickpoints along the channels, and the values of k_{sn} above and below them (also on Table 1). In these cases, channels become between 1.1 and 5 times steeper downstream of the knickpoints with respect to their upstream sections. Most catchments have at least one knickpoint (85% of the catchments along the VDF, and 87% of those along the EAF), and six catchments on the VDF (40% of the total), and three catchments on the EAF (20% of the total) have two sets of knickpoints.

For each catchment, we plot along strike the mean height of each set of knickpoints measured from the fault, and show the range of elevations as error bars (Fig. 8; Table 1). On the VDF, the single or lowest set of knickpoints are found throughout the fault length at elevations between *ca.* 150 m and *ca.* 600 m, which reach a maximum in the sector between the AL-SC and Padula segments. The upper set of knickpoints on the VDF is only found in catchments of the Polla and AL-SC segments, at elevations between 270 and 660 m. On the EAF, knickpoints are found at elevations between *ca.* 110 m and *ca.* 570 m, and reach maximum values on the area of the throw minimum between the Marsico Nuovo and the Marsicovetere segments. The upper set of knickpoints on the EAF is found at elevations between 300 m and 530 m, close to the footwall relief.

As we have excluded lithological knickpoints from our analysis, these slope-break knickpoints likely reflect base-level changes that have affected the catchments. While both basins had episodic lakes during the Pleistocene, they were not long-lived or deep enough to have generated significant high-magnitude base level changes (e.g.

Karner *et al.*, 1999; Giano, 2011; Zembo *et al.*, 2012). The hangingwall basins are filled, so there has been no abrupt base-level fall due to basin incision or drainage capture. Consequently, we argue that the most likely explanation for the existence of these knickpoints is the fact that these channels cross active faults. Moreover, given that (i) lower set of knickpoints are consistently present where catchments drain through mapped fault segment boundaries, and (ii) throw does not decay to zero at any fault segment boundaries (c.f. Papanikolaou & Roberts, 2007), a plausible explanation for the generation of these knickpoints is fault growth and linkage, which should lead to slip rate increases as fault segments interact and later link (c.f. Fig. 1).

Because the vertical component of knickpoint migration scales with the magnitude of the throw-rate perturbation experienced (e.g. Attal *et al.*, 2008; Whittaker *et al.*, 2008; Whittaker & Walker, 2015), knickpoints should be higher in the areas along the fault that have experienced greater throw rate changes (i.e. the centre of the fault and old segment boundaries; Fig. 1; Cowie & Roberts, 2001). The systematic variation in knickpoint heights along strike is consistent with this explanation and this is likely why knickpoints close to fault tips lie at low elevations (Fig. 8), because distal sectors of the fault experience the smallest throw rate changes prior, during and post-linkage, as they only have one along-strike segment neighbour to interact with (e.g. Cowie & Roberts, 2001). The upper set of knickpoints may reflect an early stage of fault linkage or fault initiation, and we analyse the significance of both these knickpoint sets in further detail in the discussion, below.

DISCUSSION

Fault throws and post-18 ka throw rates

We have reconstructed throw profiles for three Southern Apennines normal faults, and we have inferred three new post-18 ka throw rate profiles (Fig. 4). The *ca.* 2 km total throws of the Vallo di Diano and East Agri faults are the greatest reported in the Southern Apennines (c.f. Papanikolaou & Roberts, 2007). For both faults, the throw/length ratios are *ca.* 0.05, at the upper end of values reported for the Southern Apennines array (0.025–0.058; Papanikolaou & Roberts, 2007). Backstripping the total throw using post-18 ka throw rates, we obtain minimum fault initiation ages of 1.8–2 Ma for the VDF and EAF (Fig. 4). However, our evidence from the presence of non-zero throw values near fault segment boundaries, and knickpoints in the long profiles suggest that throw rates have increased as the fault segments have grown, interacted and eventually linked (Fig. 8). Consequently, the fault initiation time is probably older than 2 Ma.

The MMF has a lower total throw (*ca.* 1100 m) and throw rate values (*ca.* 0.4 mm year⁻¹), and comparatively smaller throw/length ratio (*ca.* 0.03) than the other faults (Fig. 4). Nevertheless, our maximum inferred throw rates

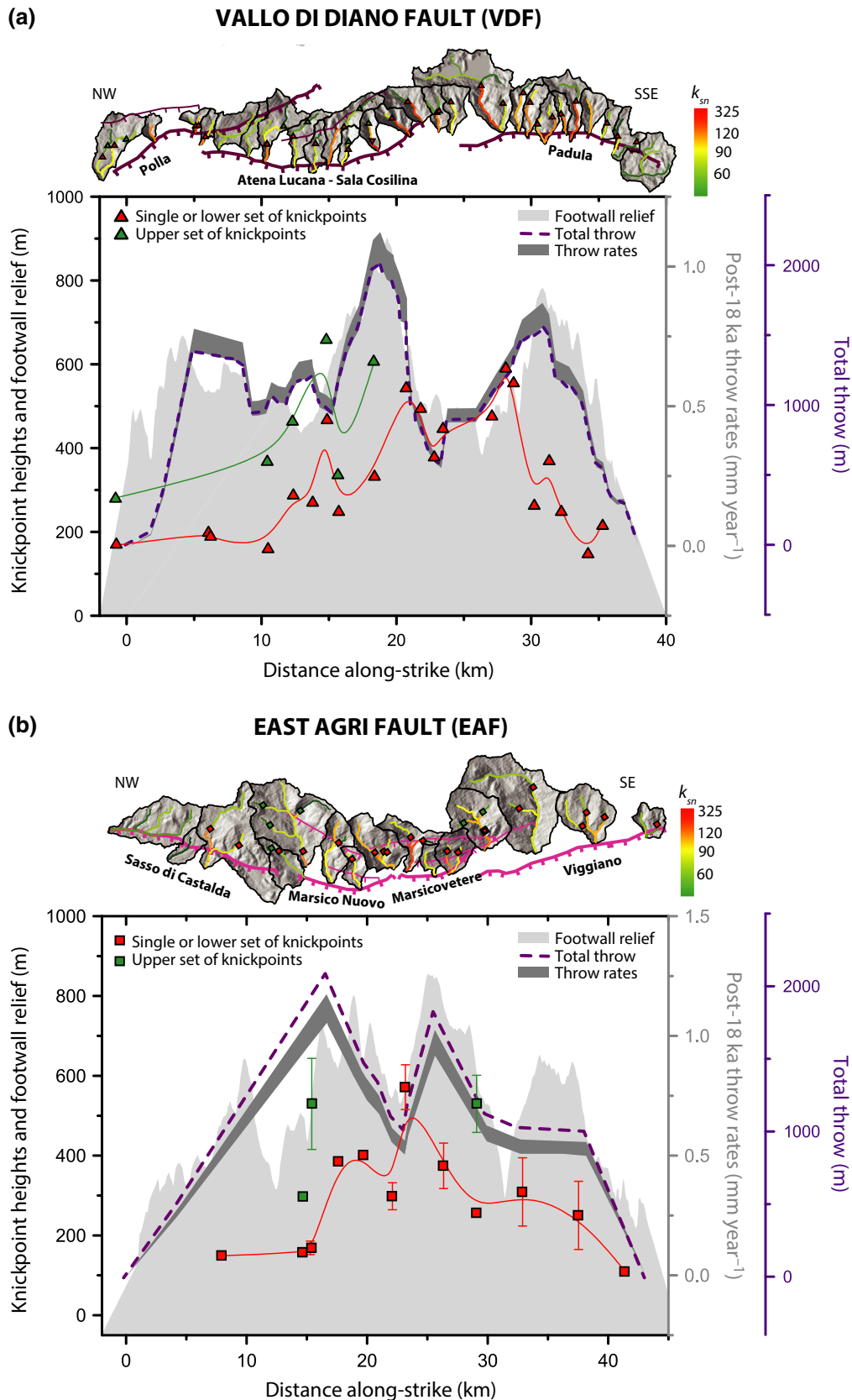


Fig. 8. Knickpoint heights measured from the basin bounding faults, shown along strike with footwall relief (grey background), total throw and post-18 ka throw rates for the VDF (a) and EAF (b). The plan-view distribution of these knickpoints is shown above the graphs, with the k_{sn} values above and below them.

are higher than Papanikolaou & Roberts (2007) suggested ($<0.2 \text{ mm year}^{-1}$) based on the estimates of Maschio *et al.* (2005), because these were collected closer to the southern fault tip than to the fault centre (Fig. 4c). A 0.75–0.18 Ma fault initiation age has been suggested by several authors (Maschio *et al.*, 2005; Zembo *et al.*, 2009, 2012; Improta *et al.*, 2010); however, all these studies are restricted to the SE fault segments. Our throw backstripping suggests a younger onset age than the other studied faults, ($1.4 \pm 0.4 \text{ Ma}$). However, a very late Pleistocene initiation of this fault is unlikely: to achieve the cumulative throw at the centre of the fault (Fig. 4c) in as little as 180 ka, fault throw rates would have to be an order of magnitude greater than reported (Schiattarella *et al.*, 2003; Maschio *et al.*, 2005). The Spinoso conglomerates, attributed an Early Pleistocene age and found adjacent to the MMF eastern branch (Zembo *et al.*, 2012), also suggest that this fault started its activity around this time. We hypothesize that the MMF nucleated at a similar time as the other studied faults, but may have had its growth inhibited by a stress shadow created by the more active VDF and EAF (e.g. Cowie, 1998; Gupta *et al.*, 1998), which would explain its subdued geomorphic expression (Figs 4c and 7c; Maschio *et al.*, 2005).

Landscape response to normal faulting for the Vallo di Diano and East Agri faults

Figures 6 and 7 show that landscape metrics of catchments eroding the footwall of the VDF and EAF correlate with measures of tectonic activity. Catchment geomorphology reflects the variation in fault slip rate along strike, with those in the centres of the faults having median slopes *ca.* 10–15° steeper than those at the fault tips (Fig. 6a–b). Catchment-averaged k_{sn} values also record the along-strike fault activity: k_{sn} values are *ca.* $100 \text{ m}^{0.9}$ greater in the fastest uplifting catchments than in those at the tips (Fig. 6a–b). The response of channels and hillslopes to tectonics is similar and both geomorphic indicators track fault activity with comparable sensitivities (Fig. 7), suggesting that incision is propagating the signal of faulting to the channels and hillslopes at a similar rate.

Couplings between k_{sn} , slope, relief and tectonic rates have been previously reported in settings that are actively uplifting (e.g. Lague & Davy, 2003; Wobus *et al.*, 2006a; Ouimet *et al.*, 2009; Cyr *et al.*, 2010; DiBiase *et al.*, 2010; Miller *et al.*, 2012). Some of these authors have found that k_{sn} and catchment slopes correlate well, in most cases non-linearly (Ouimet *et al.*, 2009; DiBiase *et al.*, 2010; Bookhagen & Strecker, 2012), which implies that channels can steepen beyond the point in which slopes are strength limited and become invariable (*ca.* 20–30°, in their studies corresponding to a k_{sn} value of *ca.* 100–150). Consequently, Ouimet *et al.* (2009) and DiBiase *et al.* (2010) concluded that channel gradients are a more faithful recorder of tectonic activity than catchment slopes as a whole. However, in our study, channels and hillslopes are still steepening at similar rates with increasing throw

rates, with catchments becoming *ca.* 1° steeper for each 10-point increase in k_{sn} value. This compares well with the below-threshold relation found by Ouimet *et al.* (2009) and Bookhagen & Strecker (2012), but is three times lower than the relation found by DiBiase *et al.* (2010) and Miller *et al.* (2013).

Densmore *et al.* (2004, 2007) found that along normal faults of the Basin and Range, relief only reflects the fault displacement profile within *ca.* 15 km of the fault tips. Beyond this, channels and hillslope slopes reach critical values marking the onset of very effective erosion, limiting footwall relief and decoupling it from the total throw profile. Consequently, relief, channel and catchment slopes are uniform in the centre of the faults, and insensitive to the along strike variations of fault activity. Our results differ because we find that the landscape (relief, channels and catchment slopes) reflects fault activity along the entire fault length; mapped fault segment boundaries correlate with minima in footwall relief, and geological measurements of high fault throw are typically located near footwall relief maxima. We suggest that the fact that topographic and channel steepness metrics both reflect fault activity is most likely because slopes have not yet surpassed the critical strength-limited threshold for hillslopes that marks the onset of landslide-dominated erosion. Field observations indicate that there is incipient shallow landsliding in flysch and sandstone outcrops so critical slopes might have been reached in some areas, but have not yet decoupled the geomorphology from the normal fault activity. Moreover, our faults are younger, shorter, and have fewer segments than those studied by Densmore *et al.* (2007), meaning that the fault centres are still relatively close to the fault tips, there is less potential for interactions, and that there has not been enough time to develop very large cumulative throws that could lead to erosional thresholds being exceeded. Figures 6 and 7 do not reveal any significant changes in landscape response to tectonics due to lithology, and instead catchments with different lithologies seem to respond similarly and fall within the same trends, as was also found by Miller *et al.* (2013) for below-threshold catchments in the Appalachians.

Fault linkage and faulting history for the Vallo di Diano and East Agri faults

While whole channel k_{sn} values and catchment averaged slopes reflect time-integrated tectonic activity along the studied faults, the presence of knickpoints on the studied channels indicates that fault throw rates have changed over time. The knickpoints also indicate that different parts of the catchments are transiently responding to differing tectonic boundary conditions, which may also explain part of the scatter in Fig. 7. Our geomorphic analysis presented above suggested two episodes of relative base-level change, which we inferred to be due to fault growth, interaction and linkage. Here we combine fault interaction theory with the total throw profiles (Fig. 4)

and the distribution of knickpoints along the fault strikes (Fig. 8) to infer possible fault segment linkage scenarios that could plausibly explain our observations.

In the VDF, the single or lower set of knickpoints is found all along the fault, reaching higher elevations in the area around the segment boundary between the AL-SC and Padula segments. This suggests that all catchments along the fault have experienced relative slip rate changes, but the sector between AL-SC and Padula segments has experienced the greater relative changes (Fig. 8a). We also observe (Fig. 9a) that between these two segments there is a throw minimum that has accumulated only *ca.* 560 m of throw (Fig. 9a). In contrast, between the Polla and the AL-SC segments, the throw minimum has accumulated *ca.* 930 m of throw, about *ca.* 370 m more. Provided that our throw rate profiles are capturing well the distribution of throw rates along strike, a good way to explain this difference is that the area between the AL-SC and Polla segments has been accumulating throw for longer than the sector between the AL-SC and Padula segments, which would imply that the former segments

linked earlier than the latter. Therefore, the single or lower set of knickpoints probably reflects a linkage event between the previously linked Polla and AL-SC segments with the Padula segment, and *ca.* 560 m of throw have been accumulated since then. The upper set of knickpoints is only found in catchments of the Polla and AL-SC segments (Fig. 8a), so it is possible that these reflect the previous linkage event between these two segments, which would have accumulated *ca.* 370 m of throw before the subsequent linkage episode (Fig. 9a).

In the EAF, we find the lower or single knickpoints all along the fault, at higher elevations around the central catchments of the fault (Fig. 8b). This distribution would agree with a single linkage event in which all segments along the fault have linked, and the centre of the fault is accommodating more of the consequent slip rate enhancement. Based on the elevation of the only throw minima that we can identify in this fault, *ca.* 1050 m of throw would have been accumulated following this linkage event (Fig. 9b). This scenario also explains the discrepancy in the centre of the fault between S_{50} and k_{sn} and total throw:

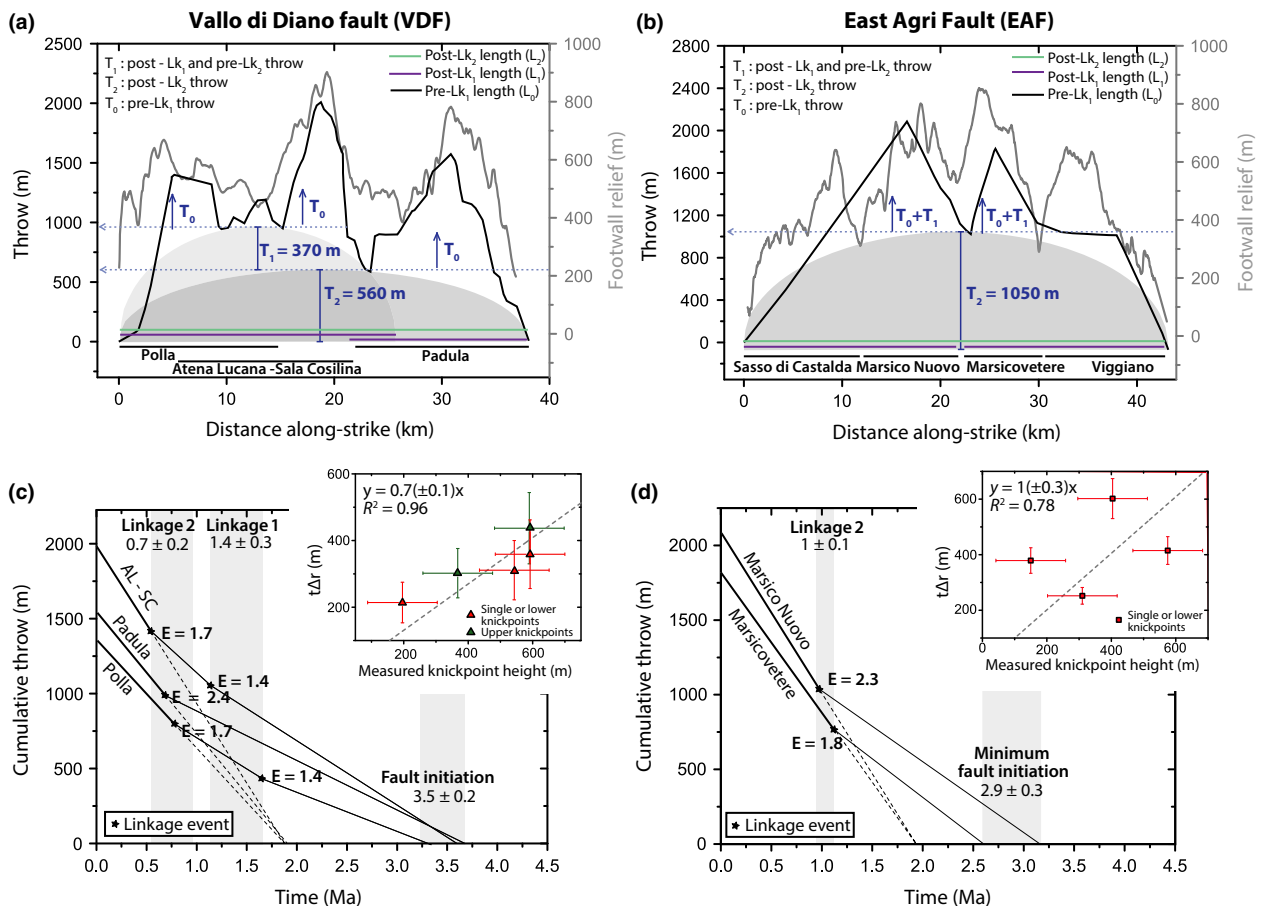


Fig. 9. Throw accumulated at each stage of fault linkage for the VDF and EAF (a–b), reconstructed faulting histories (c–d), and a comparison of the expected knickpoint heights based on theoretical considerations against the measured heights, for the highest knickpoint in each generation and fault segment (insets on c–d). Throw values from (a) and (b), and enhancement (E) and throw rate values presented in Table 2 are used to reconstruct the faulting histories in (c) and (d). On the inset graphs, the uncertainty on measured knickpoint heights reflects the smoothing window used when extracting the river long profiles (108 m), while uncertainties in Eqn 4 (y axis) are propagated from the uncertainties in the reconstructed mean values of Lk₂ and Lk₁.

catchments here are responding to the newly enhanced throw rates, but the total throw deficit that existed before the segments linked still persists (c.f. Fig. 1). An upper set of knickpoints is only found in three catchments; and it is very close to the footwall relief, so they could have been formed as faults initiated and fault-driven relief started to develop (e.g. Fig. 1, Whittaker & Walker, 2015). However, we cannot rule out the possibility that they might be related to a previous segment interaction event in which the two northern (Sasso di Castalda and Marsico Nuovo) and the two southern (Marsicovetere and Viggiano) segments linked.

Based on these plausible fault linkage scenarios, and the post-18 ka throw rates presented in Fig. 4, fault interaction theory can be used to reconstruct the possible timing of the fault linkage episodes and the associated magnitude of the throw rate perturbations. Using the mapped fault segment lengths, we calculate throw enhancement values, E , for segments of the VDF and EAF using Eqn 1 for the inferred fault linkage episodes (Table 2). For the second and youngest linkage event (Lk_2), we use L_{n-1} values corresponding to the two northern and two southern segments of each fault (L_1 ,

Fig. 9a–b), previously linked during Lk_1 , and R_n values corresponding to the fully linked fault (E_2 values, Table 2). For the first linkage event (Lk_1), L_{n-1} values correspond to individual, unlinked segments (L_0 , Fig. 9a–b), and R_n values that reflect the combined length of the segments that linked at this stage (E_1 values, Table 1). The length of post-linkage segments is not always the sum of the lengths of the previous segments, as they commonly overlap in en échelon arrays (e.g. Peacock & Sanderson, 1991; McLeod *et al.*, 2000).

On the VDF, the possible linkage between the Polla and the AL-SC (Lk_1) would have resulted in a throw rate enhancement (E_1) of about 1.4 for both segments, and we inferred earlier that *ca.* 370 m of throw (T_1) accumulated after this linkage (Fig. 9a; Table 2). This episode could have created the upper set of knickpoints that is found on some catchments along these segments (Fig. 8a), which are associated with downstream channel steepness increases of a factor of *ca.* 2 on average (Table 1). The subsequent linkage of the Polla-AL-SC linked segments with the Padula segment (Lk_2) would have produced throw rate enhancements (E_2) of about 1.7 on the previously linked segments, and about 2.4

Table 2. Enhancement values for each fault segment and fault linkage event for the VDF and EAF, input values used to calculate them, inferred past throw rate values, and inferred timing of fault linkage and faulting histories

| | Vallo di Diano fault (VDF) | | | East Agri fault (EAF) | | | |
|--|---|----------------------------------|--------|--|---------------------------|---------------------------|----------|
| | Polla | Atena Lucana-Sala Cosilina | Padula | Sasso di Castalda | Marsico Nuovo | Marsicovetere | Viggiano |
| Pre- Lk_1 , L_0 (m) | 15 400 | 15 500 | 15 800 | 13 360 | 7000 | 9800 | 15 900 |
| Post- Lk_1 , L_1 (m) | 22 000 | 22 000 | 15 800 | 20 360* | 20 360* | 25 700* | 25 700* |
| Post- Lk_2 , L_2 , final length (m) | 38 000 | 38 000 | 38 000 | 46 000 | 46 000 | 46 000 | 46 000 |
| $E_1 = 2R_1/L_0$ | 1.4 | 1.4 | n/a | 1.5* | 2.9* | 2.6* | 1.6* |
| $E_2 = 2R_2/L_1$ | 1.7 | 1.7 | 2.4 | 2.3*/1† | 2.3*/4.8† | 1.8*/4.2† | 1.8*/1† |
| r_2 , post-18 ka throw rates (mm year ⁻¹) | 0.7 | 1.1 | 0.8 | – | 1.1 | 0.9 | – |
| $r_1 = r_2/E_2$ (mm year ⁻¹) | 0.4 | 0.6 | 0.3 | – | 0.5*/0.2† | 0.5*/0.2† | – |
| $r_0 = r_1/E_1$ (mm year ⁻¹) | 0.3 | 0.4 | 0.3 | – | 0.2* | 0.2* | – |
| Post- Lk_2 cumulative throw, T_2 (m) | 560 | 560 | 560 | – | 1050 | 1050 | – |
| Post- Lk_1 cumulative throw, T_1 (m) | 370 | 370 | n/a | – | 1040 ($T_1 + T_0$) | 770 ($T_1 + T_0$) | – |
| Pre- Lk_1 cumulative throw, T_0 (m) | 480 | 1050 | 1000 | – | Unresolved | Unresolved | – |
| Time to accumulate T_2 at an r_2 rate, t_2 (Myr) | 0.8 | 0.5 | 0.7 | – | 1.0*,† | 1.1*,† | – |
| Time to accumulate T_1 at an r_1 rate, t_1 (Myr) | 0.9 | 0.6 | n/a | – | 2.2*/4.6† ($T_1 + T_0$) | 1.5*/3.4† ($T_1 + T_0$) | – |
| Time to accumulate T_0 at an r_0 rate, t_0 (Myr) | 1.6 | 2.4 | 3.0 | – | Unresolved | Unresolved | – |
| Time of Lk_2 , t_2 (Ma) | 0.7 ± 0.2 Ma (all three segments) | | | 1.0 ± 0.1 Ma*,† (all segments) | | | |
| Time of Lk_1 , $t_2 + t_1$ (Ma) | 1.4 ± 0.3 Ma (Polla and AL-SC segments) | | | Unresolved | | | |
| Time of fault initiation, $t_2 + t_1 + t_0$, (Ma) | 3.5 ± 0.2 Ma (all three segments) | | | >2.9 ± 0.3 Ma* / >5 ± 0.5 Ma† (all segments) | | | |

*If the two northern and two southern segments linked earlier.

†If all segments linked at the same time.

on the Padula segment (Table 2). This youngest linkage event (Lk₂) would have resulted in the formation of the lowest (or single) set of knickpoints (Fig. 8a), and subsequent accumulation of *ca.* 560 m of throw (T₂, Fig. 9a). The ratios of channel steepness indices below and above this lowest set of knickpoints have an average value of *ca.* 2 for the Polla and AL-SC segments, and *ca.* 3 for the Padula segment (Table 1), reflecting that the Padula segment has experienced greater slip rate changes, in agreement with the enhancement calculations.

In order for *ca.* 560 m of throw to have been accumulated at the post-Lk₂ throw rates (i.e. those presented earlier in this paper), between 0.5 and 0.8 Myr would be required, considering all linked segments (Table 2). Therefore, we hypothesize that the youngest linkage event on the VDF fault took place *ca.* 0.7 ± 0.2 Ma (Table 2; Fig. 9c). We estimate pre-Lk₂ throw rates (r₁) for each segment using Eqn 3, dividing the maximum post-18 ka (i.e. post-Lk₂) throw rate value (r₂, from Fig. 6) by the corresponding enhancement value associated with Lk₂, E₂ (Table 2, Fig. 1).

$$r_{n-1} = r_n / E_n \quad (3)$$

Under this pre-Lk₂ throw rates, between 0.6 and 0.9 Myr would be required to accumulate the *ca.* 370 m of throw that we inferred followed the linkage of the Polla and AL-SC segments (Table 2). Therefore, this first linkage event that created the upper set of knickpoints could have occurred around 1.4 ± 0.3 Ma (Table 2; Fig. 9c). We can also estimate the likely fault onset age following a similar approach. On the Padula segment, a minimum of *ca.* 1000 m of throw were accumulated before Lk₂ (the only linkage event that we can show this segment has experienced), at an r₁ rate that we can calculate with Eqn 3, which would require about 3 Myr of faulting history preceding Lk₂ (Table 2). On the Polla and AL-SC segments, a minimum *ca.* 450 m and *ca.* 1050 m of throw (T₀) were accumulated before Lk₁, respectively (Fig. 9a). Using inferred pre-Lk₁ throw rates (Eqn 3; Table 2), we can estimate that between 1.6 and 2.4 Myr would have been required by each segment, correspondingly, to accumulate these pre-Lk₁ throws. If we sum the respective times required by each segment to accumulate the pre-Lk₁, post-Lk₁, and post-Lk₂ throws, we obtain an overall estimate of fault initiation age of about 3.5 ± 0.2 Ma (Table 2; Fig. 9c).

On the EAF, we inferred earlier that *ca.* 1050 m of cumulative throw (T₂, Fig. 9b) postdate the youngest linkage event (Lk₂), which resulted in the formation of the lowest or single set of knickpoints. Based on the post-Lk₂ throw rates of the two central segments of the fault (the ones presented on Fig. 6; we only use throw rates from the two central segments because we have a much lower resolution of constraints on our throw profile for the distal segments); about 1 ± 0.1 Myr would be required to produce this throw; so Lk₂ probably occurred around 1 ± 0.1 Ma (Table 2; Fig. 9d). As we mentioned

earlier, there are two possible fault linkage scenarios for the EAF: either all segments linked at the same time (so Lk₂ was the only linkage event), or the two northern and the two southern segments had linked in a previous Lk₁ event. In Table 2, we report the enhancement values, pre-linkage throw rates and linkage times that could be predicted for these two scenarios. If all the individual segments linked during Lk₂ (results marked by a “†” in Table 2), the throw rate enhancement values on the two central segments would be between 4 and 5, while the distal segments would have experienced no enhancement at all (E = 1). This would result in pre-Lk₂ throw rates of only *ca.* 0.2 mm year⁻¹, which, in order to accumulate the pre-Lk₂ throws, would require *ca.* 4 ± 0.6 Myr. This would imply fault initiation ages older than 5 Ma, which is not plausible given that at that time, this area was still subject to compression (e.g. Cinque *et al.*, 1993; Hippolyte *et al.*, 1995; Ferranti & Oldow, 2005). Moreover, if the distal segments of the fault had experienced no enhancement, we would not expect to find any knickpoints in their catchments.

The linkage scenario in which the Sasso di Castalda and the Marsico Nuovo segments, and the Marsicovetere and Viggiano segments had linked following previous interaction (Lk₁) would result in lower enhancement values associated with the youngest linkage event, Lk₂. In this case, we obtain enhancement values of between 2.3 and 1.8 for the northern and southern segments, respectively (values marked with an asterisk in Table 2), which are in close agreement with the observed increases in channel steepness indices below the youngest knickpoints, of about a factor of *ca.* 2 (Table 1). We favour this hypothesis, which would imply pre-Lk₂ throw rates of about 0.5 mm year⁻¹ (Table 2). In the EAF, the resolution of our profile does not allow us to differentiate post-Lk₁ and pre-Lk₁ cumulative throws, which means that we cannot resolve the time when Lk₁ took place. The combined throw accumulated before the youngest linkage event (T₀ + T₁) is *ca.* 1040 m on the Marsico Nuovo segment and *ca.* 770 m on the Marsicovetere segment (Fig. 9b, Table 2). To accumulate these throws at the pre-Lk₂ rates of *ca.* 0.5 mm year⁻¹ would require about 2.2 and 1.5 Myr, respectively, which would imply an overall minimum fault onset age of about 2.9 ± 0.3 Ma (Table 2; Fig. 9d). However, an undetermined part of these pre-Lk₂ throws were accumulated at pre-Lk₁ throw rates; therefore, this is only a minimum estimate, and the EAF activity probably initiated earlier than this.

Overall, these faulting histories suggest that the VDF and EAF probably have experienced two linkage events that have resulted in subsequent throw rate enhancements and have generated knickpoints on the channels crossing the faults. We estimate that the VDF started its activity around 3.5 ± 0.2 Ma, and a minimum fault onset age of 2.9 ± 0.3 Ma for the EAF. These estimates are in close agreement with the ages of normal fault initiation for the whole Southern Apennines array suggested by

Papanikolaou & Roberts (2007). Our reconstruction of Lk₂ provides similar ages to the ca. 0.7 Ma fault interaction event inferred by Roberts & Michetti (2004) for the Central Apennines. Independently, several authors have identified a change in the intensity, style and/or orientation of the extensional stress field at ca. 0.7 Ma on the Central-Southern Apennines and Calabria (e.g. Cinque *et al.*, 1993; Hippolyte *et al.*, 1994; Amato & Montone, 1997; Patacca & Scandone, 2007).

Moreover, we can examine if the faulting histories reconstructed above are reasonable and consistent with the heights of the knickpoints that record the fault interaction events. Field data and modelling work (Wobus *et al.*, 2006b; Whittaker *et al.*, 2008) indicate that knickpoint heights upstream of faults, $H_{\text{knickpoint}}$, are proportional to the throw rate difference ($r_n - r_{n-1}$) and the time, t_n , since the perturbation took place:

$$H_{\text{knickpoint}} \sim t_n(r_n - r_{n-1}) \quad (4)$$

The coefficient of proportionality in this relationship also depends on factors such as long-term sediment aggradations in the hangingwall so Eqn 4 produces only rough estimates. We compare the highest knickpoint found in each segment of the fault (Fig. 8, Table 1) with predictions from Eqn 4. To do this, we use the mean Lk₂ and Lk₁ age estimates presented in Fig. 9c–d, and the throw rates (r_2 , r_1 and r_0) calculated for each segment and presented in Table 2. To calculate the final knickpoint heights, we use the throw rates and timing associated with each linkage interval, because throughout faulting history knickpoints have migrated vertically at different rates that relate to the magnitude of the last perturbation experienced. In the EAF, to increase the robustness of the test, we have also included the most distal segments (Sasso di Castalda and Viggiano), not used to reconstruct faulting histories.

The insets in Fig. 9c–d show statistically significant linear correlations ($R^2 = 0.96$; VDF; $R^2 = 0.78$ EAF) between the throw rate difference and time, and the heights of knickpoints presented in Fig. 8. For the EAF, measured knickpoint heights are similar to those estimated by Eqn 4, while in the VDF, measured heights are about 40% greater than the predicted values. This difference likely arises from other factors that control knickpoint migration rates which have not been considered here, such as lithology, discharge or sediment supply. Nevertheless, these correlations between measured heights and those based on the timing and magnitude of the throw rate perturbations indicate that our reconstructed faulting histories are plausible.

CONCLUSIONS

Compilation of published and new data on throw and throw rates for three normal faults in the centre of the Southern Apennines fault array (the Vallo di Diano,

Monti della Maddalena and East Agri faults) allows us to characterize landscape response to normal fault growth, and to reconstruct the faulting histories for two of these faults. Our results show total cumulative throws of ca. 2000 m for the VDF and EAF, and ca. 1100 m for the MMF. Post-glacial (i.e. post-18 ka) throw rates are up to ca. 1 mm year⁻¹ for the VDF and EAF, and ca. 0.7 mm year⁻¹ for the MMF.

For the VDF and EAF, footwall catchments are responding to normal faulting by steepening their channels and slope distributions at similar rates. Therefore, catchment geomorphology is still coupled with the tectonic forcing, and k_{sn} and catchment slopes track the along strike distribution of fault activity. In this area, lithology apparently has had a limited influence on the landscape response to normal forcing.

Because the landscape effectively records normal faulting in the VDF and EAF, we use it to reconstruct faulting histories. We identify two generations of knickpoints in channels crossing these faults, which we suggest relate to fault linkage events. Using information from our constructed total throw profiles, post-18 ka throw rates, and fault interaction theory, we estimate that these linkage events took place at 0.7 ± 0.2 Ma and 1.4 ± 0.3 Ma for the VDF, and 1 ± 0.1 for the EAF. These faulting histories suggest an overall fault initiation age of 3.5 ± 0.2 Ma for the VDF, and a minimum age of 2.9 ± 0.3 Ma for the EAF, and are consistent with the knickpoint height distributions, and independent geological constraints of the timing of extension in the Southern Apennines.

ACKNOWLEDGEMENTS

DRB was supported by an Imperial College Janet Watson Bursary, and acknowledges the Geological Society of London and the British Society for Geomorphology (BSG) for their support. The authors would like to thank the editor, George Hillel, Nancye Dawers, and two anonymous reviewers for their constructive comments which helped us improve the manuscript.

CONFLICT OF INTEREST

No conflict of interest declared.

REFERENCES

- AMATO, A. & MONTONE, P. (1997) Present-day stress field and active tectonics in southern peninsular Italy. *Geophys. J. Int.*, **130**, 519–534.
- AMICUCCI, L., BARCHI, M.R., MONTONE, P. & RUBILIANI, N. (2008) The Vallo Di Diano and Auletta extensional basins in the Southern Apennines (Italy): a simple model for a complex setting. *Terra Nova*, **20**, 475–482.

- ANDERS, M.H. & SCHLISCHE, R.W. (1994) Overlapping faults, intrabasin highs, and the growth of normal faults. *J. Geol.*, **102**, 165–179.
- ANDERS, M.H., SPIEGELMAN, M., RODGERS, D.W. & HAGSTRUM, J.T. (1993) The growth of fault-bounded tilt blocks. *Tectonics*, **12**, 1451–1459.
- ATTAL, M., TUCKER, G., WHITTAKER, A., COWIE, P. & ROBERTS, G.P. (2008) Modeling fluvial incision and transient landscape evolution: influence of dynamic channel adjustment. *J. Geophys. Res. Series F*, **113**.
- ATTAL, M., COWIE, P., WHITTAKER, A., HOBLEY, D., TUCKER, G. & ROBERTS, G.P. (2011) Testing fluvial erosion models using the transient response of bedrock rivers to tectonic forcing in the Apennines, Italy. *J. Geophys. Res. Series F*, **116**.
- BARCHI, M., AMATO, A., CIPPITELLI, G., ENI, D.A., SAN DONATO MILANESE, M., MERLINI, S. & MONTONE, P. (2006) Extensional tectonics and seismicity in the axial zone of the Southern Apennines. *Boll. Soc. Geol. It.*
- BENEDETTI, L., TAPPONNIER, P., KING, G. & PICCARDI, L. (1998) Surface rupture of the 1857 Southern Italian Earthquake? *Terra Nova*, **10**, 206–210.
- BOOKHAGEN, B. & STRECKER, M.R. (2012) Spatiotemporal trends in erosion rates across a pronounced rainfall gradient: examples from the Southern Central Andes. *Earth Planet. Sci. Lett.*, **327**, 97–110.
- BOULTON, S.J. & WHITTAKER, A.C. (2009) Quantifying the slip rates, spatial distribution and evolution of active normal faults from geomorphic analysis: field examples from an oblique-extensional Graben, Southern Turkey. *Geomorphology*, **104**, 299–316.
- BRUNO, P.P., CASTIELLO, A., VILLANI, F. & IMPROTA, L. (2013) High-resolution densely spaced wide-aperture seismic profiling as a tool to aid seismic hazard assessment of fault-bounded intramontane basins: application to Vallo Di Diano, Southern Italy. *Bull. Seismol. Soc. Am.*, **103**, 1969–1980.
- CARTWRIGHT, J.A., MANSFIELD, C. & TRUDGILL, B. (1996) The growth of normal faults by segment linkage. *Geol. Soc. London Spec. Publ.*, **99**, 163–177.
- CARTWRIGHT, J.A., TRUDGILL, B.D. & MANSFIELD, C.S. (1995) Fault growth by segment linkage: an explanation for scatter in maximum displacement and trace length data from the canyonlands Grabens of Se Utah. *J. Struct. Geol.*, **17**, 1319–1326.
- CELLO, G., TONDI, E., MICARELLI, L. & MATTIONI, L. (2003) Active tectonics and earthquake sources in the epicentral area of the 1857 Basilicata Earthquake (Southern Italy). *J. Geodyn.*, **36**, 37–50.
- CINQUE, A., PATACCA, E., SCANDONE, P. & TOZZI, M. (1993) Quaternary kinematic evolution of the Southern Apennines. Relationships between surface geological features and deep lithospheric structures. *Ann. Geophys.*, **36**, 249–260.
- CINQUE, A., ASCIONE, A. & CALAZZO, C. (2000) Distribuzione Spazio-Temporale E Caratterizzazione Della Fagliazione Quaternaria in Appennino Meridionale. *Le Ricerche del GNDT nel Campo Della Pericolosità Sismica (1996 E1999)*. CNR-GNDT, Rome, pp. 203–218 (in Italian).
- COLELLA, A., LAPENNA, V. & RIZZO, E. (2004) High-resolution imaging of the high agri Valley Basin (Southern Italy) with electrical resistivity tomography. *Tectonophysics*, **386**, 29–40.
- COMMIN, D., GUPTA, S. & CARTWRIGHT, J. (2005) Deformed streams reveal growth and linkage of a normal fault array in the Canyonlands Graben, Utah. *Geology*, **33**, 645–648.
- COWIE, P. (1998) A healing-reloading feedback control on the growth rate of seismogenic faults. *J. Struct. Geol.*, **20**, 1075–1087.
- COWIE, P.A. & ROBERTS, G.P. (2001) Constraining slip rates and spacings for active normal faults. *J. Struct. Geol.*, **23**, 1901–1915.
- COWIE, P.A. & SCHOLZ, C.H. (1992a) Physical explanation for the displacement-length relationship of faults using a post-yield fracture mechanics model. *J. Struct. Geol.*, **14**, 1133–1148.
- COWIE, P.A. & SCHOLZ, C.H. (1992b) Displacement-length scaling relationship for faults: data synthesis and discussion. *J. Struct. Geol.*, **14**, 1149–1156.
- COWIE, P., ATTAL, M., TUCKER, G., WHITTAKER, A., NAYLOR, M., GANAS, A. & ROBERTS, G. (2006) Investigating the surface process response to fault interaction and linkage using a numerical modelling approach. *Basin Res.*, **18**, 231–266.
- CROSBY, B.T. & WHIPPLE, K.X. (2006) Knickpoint initiation and distribution within fluvial networks: 236 Waterfalls in the Waipaoa River, North Island, New Zealand. *Geomorphology*, **82**, 16–38.
- CYR, A.J., GRANGER, D.E., OLIVETTI, V. & MOLIN, P. (2010) Quantifying rock uplift rates using channel steepness and cosmogenic nuclide-determined erosion rates: examples from Northern and Southern Italy. *Lithosphere*, **2**, 188–198.
- D'ARCY, M. & WHITTAKER, A.C. (2014) Geomorphic constraints on landscape sensitivity to climate in tectonically active areas. *Geomorphology*, **204**, 366–381.
- DAWERS, N.H. & ANDERS, M.H. (1995) Displacement-length scaling and fault linkage. *J. Struct. Geol.*, **17**, 607–614.
- DENSMORE, A.L., DAWERS, N.H., GUPTA, S., GUIDON, R. & GOLDIN, T. (2004) Footwall topographic development during continental extension. *J. Geophys. Res. Series F*, **109**.
- DENSMORE, A.L., LI, Y., ELLIS, M.A. & ZHOU, R. (2005) Active tectonics and erosional unloading at the eastern margin of the Tibetan Plateau. *J. Mt. Sci.*, **2**, 146–154.
- DENSMORE, A.L., ALLEN, P.A. & SIMPSON, G. (2007) Development and response of a coupled catchment fan system under changing tectonic and climatic forcing. *J. Geophys. Res. Series F*, **112**.
- DI BIASE, R.A., WHIPPLE, K.X., HEIMSATH, A.M. & OUMET, W.B. (2010) Landscape form and millennial erosion rates in the San Gabriel Mountains, Ca. *Earth Planet. Sci. Lett.*, **289**, 134–144.
- FAURE-WALKER, J., ROBERTS, G.P., COWIE, P., PAPANIKOLAOU, I.D., SAMMONDS, P., MICHETTI, A. & PHILLIPS, R. (2009) Horizontal strain-rates and throw-rates across breached relay zones, central Italy: implications for the preservation of throw deficits at points of normal fault linkage. *J. Struct. Geol.*, **31**, 1145–1160.
- FERRANTI, L. & OLDOW, J.S. (2005) Latest miocene to quaternary horizontal and vertical displacement rates during simultaneous contraction and extension in the Southern Apennines Orogen, Italy. *Terra Nova*, **17**, 209–214.
- FERRANTI, L., PALANO, M., CANNAVÒ, F., MAZZELLA, M.E., OLDOW, J.S., GUEGUEN, E., MATTIA, M. & MONACO, C. (2014) Rates of geodetic deformation across active faults in Southern Italy. *Tectonophysics*, **621**, 101–122.

- FINNEGAN, N.J., ROE, G., MONTGOMERY, D.R. & HALLET, B. (2005) Controls on the channel width of rivers: implications for modeling fluvial incision of bedrock. *Geology*, **33**, 229–232.
- GIANO, S.I. (2011) Quaternary alluvial fan systems of the agri intermontane Basin (Southern Italy): tectonic and climatic controls. *Geol. Carpath.*, **62**, 65–76.
- GIANO, S., GIOIA, D., LAURENZI, M.A. & SCHIATTARELLA, M. (2014) Nuovi vincoli su età, entità e velocità delle dislocazioni quaternarie nell'area del Vallo Di Diano (Appennino meridionale). *Dialogo Intorno al Paesaggio. Percezione, Interpretazione Rappresentazione. Culture Territori Linguaggi*, **4**, 159–173.
- GIACOLI, A., STABILE, T., ADURNO, I., PERRONE, A., GALLIPOLI, M., GUEGUEN, E., NORELLI, E. & PISCITELLI, S. (2015) Geological and geophysical characterization of the South-Eastern side of the high agri valley (Southern Apennines, Italy). *Nat. Haz. Ear. Sys. Sci.*, **15**, 315–323.
- GUPTA, A. & SCHOLZ, C.H. (2000) A model of normal fault interaction based on observations and theory. *J. Struct. Geol.*, **22**, 865–879.
- GUPTA, S., COWIE, P.A., DAWERS, N.H. & UNDERHILL, J.R. (1998) A mechanism to explain rift-basin subsidence and stratigraphic patterns through fault-array evolution. *Geology*, **26**, 595–598.
- HIPPOLYTE, J.-C., ANGELIER, J. & ROURE, F. (1994) A major geodynamic change revealed by quaternary stress patterns in the Southern Apennines (Italy). *Tectonophysics*, **230**, 199–210.
- HIPPOLYTE, J.-C., ANGELIER, J. & BARRIER, E. (1995) Compressional and extensional tectonics in an arc system: example of the Southern Apennines. *J. Struct. Geol.*, **17**, 1725–1740.
- HOPKINS, M.C. & DAWERS, N.H. (2015) Changes in bedrock channel morphology driven by displacement rate increase during normal fault interaction and linkage. *Basin Res.*, **27**(1), 43–59.
- IMPROTA, L., FERRANTI, L., de MARTINI, P., PISCITELLI, S., BRUNO, P., BURRATO, P., CIVICO, R., GIACOLI, A., IORIO, M. & D'ADDEZIO, G. (2010) Detecting young, slow-slipping active faults by geologic and multidisciplinary high-resolution geophysical investigations: a case study from the Apennine Seismic Belt, Italy. *J. Geophys. Res.*, **115**, B11307.
- KARNER, D., JUVIGNE, E., BRANCACCIO, L., CINQUE, A., RUSSO ERMOLLI, E., SANTANGELO, N., BERNASCONI, S. & LIRER, L. (1999) A potential early middle pleistocene tephrostratotype for the Mediterranean Basin: The Vallo Di Diano, Campania, Italy. *Global Planet. Change*, **21**, 1–15.
- KING, G.C., STEIN, R.S. & RUNDLE, J.B. (1988) The growth of geological structures by repeated earthquakes 1. Conceptual framework. *J. Geophys. Res. Solid Earth*, (1978–2012), **93**, 13307–13318.
- KIRBY, E. & WHIPPLE, K.X. (2012) Expression of active tectonics in erosional landscapes. *J. Struct. Geol.*, **44**, 54–75.
- LAGUE, D. & DAVY, P. (2003) Constraints on the long-term coluvial erosion law by analyzing slope-area relationships at various tectonic uplift rates in the Siwaliks Hills (Nepal). *J. Geophys. Res., Solid Earth* (1978–2012), **108**. doi:10.1029/2002JB001893.
- MASCHIO, L., FERRANTI, L. & BURRATO, P. (2005) Active extension in Val D'agri Area, Southern Apennines, Italy: implications for the geometry of the seismogenic belt. *Geophys. J. Int.*, **162**, 591–609.
- MCLEOD, A.E., DAWERS, N.H. & UNDERHILL, J.R. (2000) The propagation and linkage of normal faults: insights from the strathspey–brent–statfjord fault array, Northern North Sea. *Basin Res.*, **12**, 263–284.
- MILLER, S.R., BALDWIN, S.L. & FITZGERALD, P.G. (2012) Transient fluvial incision and active surface uplift in the woodlark rift of Eastern Papua New Guinea. *Lithosphere*, **4**, 131–149.
- MILLER, S.R., SAK, P.B., KIRBY, E. & BIERMAN, P.R. (2013) Neogene rejuvenation of central Appalachian topography: evidence for differential rock uplift from stream profiles and erosion rates. *Earth Planet. Sci. Lett.*, **369**, 1–12.
- MIRABELLA, F., CIACCIO, M., BARCHI, M. & MERLINI, S. (2004) The gubbio normal fault (Central Italy): geometry, displacement distribution and tectonic evolution. *J. Struct. Geol.*, **26**, 2233–2249.
- MONTGOMERY, D.R. & BRANDON, M.T. (2002) Topographic controls on erosion rates in tectonically active mountain ranges. *Earth Planet. Sci. Lett.*, **201**, 481–489.
- NIEMANN, J.D., GASPARINI, N.M., TUCKER, G.E. & BRAS, R.L. (2001) A quantitative evaluation of Playfair's law and its use in testing long-term stream erosion models. *Earth Surf. Proc. Land.*, **26**, 1317–1332.
- OLDOW, J.S., D'ARGENIO, B., FERRANTI, L., PAPPONE, G., MARSELLA, E. & SACCHI, M. (1993) Large-scale longitudinal extension in the southern Apennines contractional belt, Italy. *Geology*, **21**, 1123–1126.
- OUMET, W.B., WHIPPLE, K.X. & GRANGER, D.E. (2009) Beyond threshold hillslopes: channel adjustment to base-level fall in tectonically active mountain ranges. *Geology*, **37**, 579–582.
- PALUMBO, L., BENEDETTI, L., BOURLÈS, D., CINQUE, A. & FINKEL, R. (2004) Slip history of the Magnola fault (Apennines, Central Italy) from ³⁶Cl surface exposure dating: evidence for strong earthquakes over the Holocene. *Earth Planet. Sci. Lett.*, **225**, 163–176.
- PANTOSTI, D. & VALENSISE, G. (1990) Faulting mechanism and complexity of the November 23, 1980, Campania-Lucania Earthquake, inferred from surface observations. *J. Geophys. Res. Solid Earth*, **95**, 15319–15341.
- PAPANIKOLAOU, I.D. & ROBERTS, G.P. (2007) Geometry, kinematics and deformation rates along the active normal fault system in the Southern Apennines: implications for fault growth. *J. Struct. Geol.*, **29**, 166–188.
- PAPANIKOLAOU, I.D., ROBERTS, G.P., DELIGIANNAKIS, G., SAKELLARIOU, A. & VASSILAKIS, E. (2013) The sparta fault, Southern Greece: from segmentation and tectonic geomorphology to seismic hazard mapping and time dependent probabilities. *Tectonophysics*, **597**, 85–105.
- PATACCA, E. & SCANDONE, P. (2007) Constraints on the Interpretation of the Crop-04 Seismic Line Derived from Plio–Pleistocene Foredeep and Thrust-Sheet-Top Deposits (Southern Apennines, Italy). CROP-04. (Ed. by Mazzotti A., Patacca E. & Scandone, P.) *Boll. della Soc. Geol. It. Special*, 241–256.
- PEACOCK, D. & SANDERSON, D. (1991) Displacements, segment linkage and relay ramps in normal fault zones. *J. Struct. Geol.*, **13**, 721–733.
- ROBERTS, G.P. & MICHETTI, A.M. (2004) Spatial and temporal variations in growth rates along active normal fault systems: an example from the Lazio–Abruzzo Apennines, Central Italy. *J. Struct. Geol.*, **26**, 339–376.
- ROBERTS, G.P., COWIE, P., PAPANIKOLAOU, I. & MICHETTI, A.M. (2004) Fault scaling relationships, deformation rates and seismic hazards: an example from the Lazio–Abruzzo Apennines, Central Italy. *J. Struct. Geol.*, **26**, 377–398.

- SANTANGELO, N. (1991) *Evoluzione Stratigrafica, Geomorfologica E Neotettonica Di Alcuni Bacini Lacustri Del Confine Campano Lucano (Italia Meridionale): Tesi Di Dottorato*. PhD thesis. Naples University "Federico II", 1991. 109 pp.
- SCHIATTARELLA, M., DI LEO, P., BENEDEUCE, P. & IVO GIANO, S. (2003) Quaternary uplift vs tectonic loading: a case study from the Lucanian Apennine, Southern Italy. *Quatern. Int.*, **101**, 239–251.
- SCHLAGENHAUF, A., MANIGHETTI, I., BENEDETTI, L., GAUDEMER, Y., FINKEL, R., MALAVIELLE, J. & POU, K. (2011) Earthquake supercycles in Central Italy, inferred from 36 Cl exposure dating. *Earth Planet. Sci. Lett.*, **307**, 487–500.
- SCHMIDT, K.M. & MONTGOMERY, D.R. (1995) Limits to relief. *Science*, **270**, 617.
- SCHOLZ, C.H. & CONTRERAS, J.C. (1998) Mechanics of continental rift architecture. *Geology*, **26**, 967–970.
- SKLAR, L.S. & DIETRICH, W.E. (2001) Sediment and rock strength controls on river incision into bedrock. *Geology*, **29**, 1087–1090.
- SNYDER, N.P., WHIPPLE, K.X., TUCKER, G.E. & MERRITTS, D.J. (2000) Landscape response to tectonic forcing: digital elevation model analysis of stream profiles in the mendocino triple junction region, Northern California. *Geol. Soc. Am. Bull.*, **112**, 1250–1263.
- SNYDER, N.P., WHIPPLE, K.X., TUCKER, G.E. & MERRITTS, D.J. (2003) Channel response to tectonic forcing: field analysis of stream morphology and hydrology in the mendocino triple junction region, Northern California. *Geomorphology*, **53**, 97–127.
- SOLIVA, R., BENEDICTO, A., SCHULTZ, R., MAERTEN, L. & MICARELLI, L. (2008) Displacement and interaction of normal fault segments branched at depth: implications for fault growth and potential earthquake rupture size. *J. Struct. Geol.*, **30**, 1288–1299.
- SPINA, V., TONDI, E., GALLI, P., MAZZOLI, S. & CELLO, G. (2008) Quaternary fault segmentation and interaction in the epicentral area of the 1561 earthquake (Mw= 6.4), Vallo Di Diano, Southern Apennines, Italy. *Tectonophysics*, **453**, 233–245.
- STEIN, R.S., KING, G.C. & RUNDLE, J.B. (1988) The growth of geological structures by repeated earthquakes 2. Field examples of continental dip-slip faults. *J. Geophys. Res. Solid Earth*, **93**, 13319–13331.
- STRAK, V., DOMINGUEZ, S., PETTIT, C., MEYER, B. & LOGET, N. (2011) Interaction between normal fault slip and erosion on relief evolution: insights from experimental modelling. *Tectonophysics*, **513**, 1–19.
- VALOROSO, L., IMPROTA, L., CHIARALUCE, L., di STEFANO, R., FERRANTI, L., GOVONI, A. & CHIARABBA, C. (2009) Active faults and induced seismicity in the Val D'agri Area (Southern Apennines, Italy). *Geophys. J. Int.*, **178**, 488–502.
- VILLANI, F. & PIERDOMINICI, S. (2010) Late quaternary tectonics of the Vallo Di Diano Basin (Southern Apennines, Italy). *Quatern. Sci. Rev.*, **29**, 3167–3183.
- WHIPPLE, K.X. & TUCKER, G.E. (1999) Dynamics of the stream-power river incision model: implications for height limits of mountain ranges, landscape response timescales, and research needs. *J. Geophys. Res. Solid Earth*, **104**, 17661–17674.
- WHIPPLE, K.X. & TUCKER, G.E. (2002) Implications of sediment-flux-dependent river incision models for landscape evolution. *J. Geophys. Res.*, **107**, 2039.
- WHITTAKER, A.C. (2012) How do landscapes record tectonics and climate? *Lithosphere*, **4**, 160–164.
- WHITTAKER, A.C. & BOULTON, S.J. (2012) Tectonic and climatic controls on knickpoint retreat rates and landscape response times. *J. Geophys. Res. Series F*, **117**.
- WHITTAKER, A.C. & WALKER, A.S. (2015) Geomorphic constraints on fault throw rates and linkage times: examples from the Northern Gulf of Evia, Greece. *J. Geophys. Res. Series F*, **120**, 137–158.
- WHITTAKER, A.C., COWIE, P.A., ATTAL, M., TUCKER, G.E. & ROBERTS, G.P. (2007) Contrasting transient and steady-state rivers crossing active normal faults: new field observations from the Central Apennines, Italy. *Basin Res.*, **19**, 529–556.
- WHITTAKER, A.C., ATTAL, M., COWIE, P.A., TUCKER, G.E. & ROBERTS, G. (2008) Decoding temporal and spatial patterns of fault uplift using transient river long profiles. *Geomorphology*, **100**, 506–526.
- WHITTAKER, A.C., ATTAL, M. & ALLEN, P.A. (2010) Characterising the origin, nature and fate of sediment exported from catchments perturbed by active tectonics. *Basin Res.*, **22**, 809–828.
- WOBUS, C., WHIPPLE, K.X., KIRBY, E., SNYDER, N., JOHNSON, J., SPYROPOLOU, K., CROSBY, B. & SHEEHAN, D. (2006a) Tectonics from topography: procedures, promise, and pitfalls. *Spec. Pap. Geol. Soc. Am.*, **398**, 55.
- WOBUS, C.W., CROSBY, B.T. & WHIPPLE, K.X. (2006b) Hanging valleys in fluvial systems: controls on occurrence and implications for landscape evolution. *J. Geophys. Res. Series F*, **111**.
- ZEMBO, I., PANZERI, L., GALLI, A., BERSEZIO, R., MARTINI, M. & SIBILIA, E. (2009) Quaternary evolution of the intermontane Val D'agri Basin, Southern Apennines. *Quatern. Res.*, **72**, 431–442.
- ZEMBO, I., TROMBINO, L., BERSEZIO, R., FELLETTI, F. & DAPIAGGI, M. (2012) Climatic and tectonic controls on pedogenesis and landscape evolution in a quaternary intramontane basin (Val D'agri Basin, Southern Apennines, Italy). *J. Sediment. Res.*, **82**, 283–309.

Manuscript received 19 September 2015; In revised form 28 July 2016; Manuscript accepted 1 August 2016.